Materials Science and Engineering, 33 (2001) 1–50

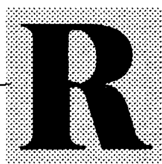

Reports: A Review Journal

www.elsevier.com/locate/mser

Near-field scanning optical microscopy studies of electronic and photonic materials and devices

Julia W.P. Hsu*

Bell Labs, Lucent Technologies, 1-D-368, 600-700 Mountain Avenue, Murray Hill, NJ 07974, USA

Accepted 15 December 2000

Abstract

Probing optical properties of materials and optical characterization of crystallographic defects at the nanometer scale have been inaccessible until recently due to the diffraction limit of light. With the invention of near-field scanning optical microscopy (NSOM), resolution at the 50–100 nm level using visible or near infrared light is now practical. In addition to describing the NSOM technique, this review focuses on the application of NSOM to the characterization of electronic and photonic materials and devices, with particular emphasis on defects. The unique capability of NSOM to simultaneously measure surface topography and local optoelectronic properties, thereby eliminating the need to perform cross correlation analysis on results obtained using different techniques, is particularly useful in this area. Several examples are discussed. By performing near-field photocurrent (NPC) measurements, NSOM is used to probe electrical activities associated with individual threading dislocations and dislocation networks in strain relaxed, compositionally graded GeSi films. The non-destructive nature of NSOM helps elucidate how microstructural defects in the $SrTiO_3$ bicrystal substrates affect $YBa_2Cu_3O_7$ film growth and GBJJ performance. Characterization of III–V and II–VI semiconductors, guantum dots grown by strain epitaxy, laser diodes, waveguides, and photonic crystals is also included. The advantages and disadvantages of NSOM in each application will be outlined. Throughout the review, emphasis is placed on how NSOM complements existing materials characterization techniques, as well as how quantitative results can be obtained from NSOM measurements. © 2001 Elsevier Science B.V. All rights reserved.

Keywords: Near-field scanning optical microscopy; Defect electronic properties; Strain; Semiconductors; Perovskite oxides; Photonic materials and devices

1. Introduction

Driven by the desire to study nanometer scale phenomena and to characterize ever-smaller devices, many variations of scanning probe microscopes were developed following the invention of the scanning tunneling microscope (STM) [1,2] and the scanning atomic force microscope (AFM or SFM) [3]. Some examples are scanning capacitance microscopy [4,5], electrostatic force microscopy [6,7], and magnetic force microscopy [8,9]. The near-field scanning optical microscope (NSOM) or scanning near-field optical microscope (SNOM) [10,11] is a scanning probe based technique that can measure local optical and/or optoelectronic properties with sub-diffraction limit resolution. Since the resolution of NSOM does not depend on the wavelength of the light, visible and near infrared light can be used, making it a true optical microscope. The availability of these new scanning probe microscopes opens up fields of studies that were previously inaccessible.

* Tel.: +1-908-582-2074; fax: +1-908-582-3260.
E-mail address: jhsu@lucent.com (J.W.P. Hsu).

0927-796X/01/$ – see front matter © 2001 Elsevier Science B.V. All rights reserved.
PII: S0927-796X(00)00031-0

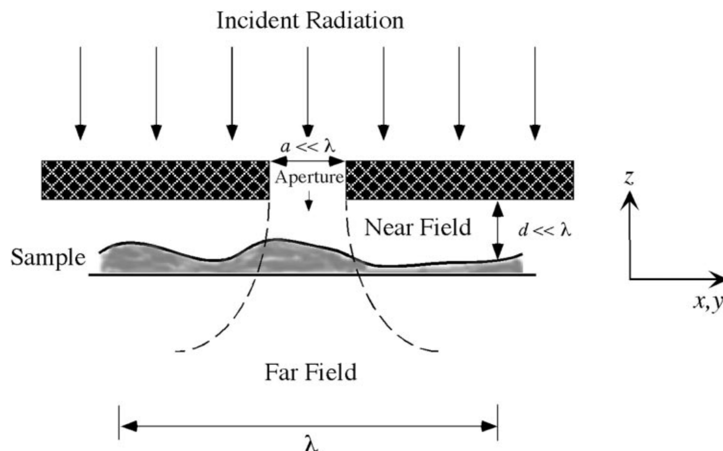

Fig. 1. A sketch showing the basic principles of sub-wavelength resolution in near-field optics. The two critical requirements are: (1) a sub-wavelength light source (aperture in the illustration), and (2) placing the sample in the near-field zone of the light source. The Cartesian coordinates used in this review are shown [28].

The basic principles behind how NSOM achieves resolution higher than the diffraction limit are illustrated in Fig. 1. A sub-wavelength-sized light source, e.g. an aperture, is placed within the near-field zone (distance much less than the wavelength) of the sample. In this case, the area of the sample illuminated is determined by the aperture size and not by the wavelength of light. An image can then be formed by moving the sample and the light source with respect to each other. This idea was first proposed by E.H. Synge in 1928 [12]. In this paper, he also pointed out the two major obstacles that would prevent the realization of a visible light NSOM for another 60 years. They are: (1) the difficulty in making a subwavelength size light source that is bright enough and (2) the difficulty in bringing a sample to the near-field zone of such a light source due to the surface roughness of usual materials. These problems were not solved until the invention of scanning probe techniques in 1980s. However, as early as 1972, the ability of near-field imaging to produce sub-diffraction limit resolution was demonstrated in microwaves, where a resolution of $\lambda/60$ was achieved with 3 cm wavelength (λ) electromagnetic waves [13].

The modern field of NSOM began with the photon scanning tunneling microscope (PSTM) [14,15]. PSTM works by probing the changes in evanescent fields of the total internal reflecting light inside a glass prism due to the sample deposited on top of the prism. The light is collected with a tapered pipette or fiber tip. A different approach involves subwavelength light sources. These were made by coating pulled pipette tips with metals, and can be used for sending light through the apertures at the end (illumination mode) or collecting light from a small region of the sample (collection mode). Since the transmission efficiency of these early tips was really low, the resolution was compromised in order to obtain sufficient signal. In 1991, a break-through in fabricating bright subwavelength apertures was demonstrated by pulling and coating single mode optical fibers [16]. Aperture sizes of 100 nm or less are now practical and routine for light of wavelength between 400 nm and 1.5 μm. Soon after, a reliable feedback method based on detection of the force interaction between the laterally vibrating NSOM tip and sample surface was introduced [17,18]. Using this distance regulation, a topographic image similar to that obtained by a conventional scanning force microscope (SFM) is acquired simultaneously with the optical image. This provides a way to correlate structural and physical properties at the same sample positions and greatly simplifies interpretation of the NSOM data. These two crucial developments

allowed NSOM to become one of the most commonly used scanning probe microscopies today. The instrumentation and functions of a present day NSOM system is reviewed in Section 2 of this article.

Optical microscopy still has many advantages over the newer, albeit higher resolution, electron microscopy. It is easy to use, requires minimal sample preparation, and can be operated in ambient or liquid environments. The power of optical microscopy lies in the various spectroscopy techniques that enable us to probe different materials properties. The contrast we see, hence the information we obtain, depends on how the microscope is operated. NSOM has inherited all the advantages of optical microscopy, including various forms of spectroscopy. In addition to nanometer resolution, single molecule sensitivity has been demonstrated [19,20]. As in conventional optical microscopes, NSOM can be operated in transmission mode in which the light source and detector are on opposite sides of the sample, and in reflection mode in which the two are on the same side of the sample. Using a tapered optical fiber as the NSOM tip, when operating in illumination mode, laser light is coupled into the cleaved, untapered end of the fiber and emerges out of the sub-wavelength aperture at the end of the tapered tip. In collection mode, light is coupled into the fiber through the sub-wavelength aperture and must convert to the propagating mode inside the fiber to reach the detector. Some authors use the term PSTM instead of “NSOM” to describe using NSOM in collection mode to study guided waves. In reflection, the probe can be used simultaneously as an illumination source and a collector.

Many review articles [21–25] and books [26,27] have been published on NSOM. Most of them focus on organic and biological applications [23,25]. Only a few of them touch upon applications in semiconductors, but in a few selected areas [22,28]. In this article, I will review the use of NSOM to characterize a broad range of electronic and photonic materials and devices. I aim to provide an introduction to researchers interested in applying NSOM to study materials. While the potential usefulness of NSOM in the biological field may be more obvious, there are also many ways NSOM can contribute to materials science. We will see that the 100 nm resolution afforded by the current NSOM has enabled researchers to study optical phenomena at unprecedented length scales. The results have already brought new knowledge and new insight into this sub-field of materials sciences and engineering. NSOM is now a mainstay in nanometer scale materials characterization.

Section 2 of this review discusses the tips and the shear force feedback commonly used in current NSOM systems. In addition, we will review the different forms of spectroscopies that can be performed using an NSOM, as well as the control of polarization and operation in non-ambient environments. Section 3 summarizes works using NSOM as the excitation source for electron–hole generation in order to study carrier dynamics in GeSi thin films. While the principle of operation is similar to electron beam-induced current (EBIC) and photocurrent imaging, the employment of NSOM produces super high resolution near electrically active defects that cannot be achieved with existing methods. Polarization control and temperature dependence shed light into the physical origins of observed NPC contrast. Section 4 describes the use of NSOM to understand the performance variations in commonly used high temperature superconductor (HTSC) grain boundary junctions. It also demonstrates how NSOM can be used to map out strain field patterns with 100 nm resolution. Section 5 reviews NSOM studies on a variety of semiconductor systems, including III-nitride materials, spontaneous order in (GaIn)P system, polycrystalline II–VI thin films, and semiconductor quantum dots (QDs). Section 6 reviews applications in photonic devices and materials, including laser diodes, waveguides, and photonic crystals. An example of difficulty in interpreting contrast in NSOM images will be elucidated in Section 7. Summary and directions for future work are given in the last section.

2. NSOM system

An NSOM system is similar to any other scanning probe microscope. It primarily consists of a tip, in this case a subwavlength light source or detector, and a scanning system to move the tip with respect to the sample with sub-nanometer precision. A feedback mechanism is employed to keep tip–sample separation constant and in the near-field regime. A computer controls and synchronizes the data acquisition to the scanning. For NSOM, an external laser and a sensitive optical detection system, which are chosen depending on the specific applications, are added to complete the system. Typically the NSOM head is incorporated in a conventional far-field optical microscope. This allows the positioning of the NSOM tip on the part of the sample of interest. NSOM, therefore, acts as the highest magnification of the entire optical microscope system.

2.1. Tapered fiber optic tips

Most commonly used NSOM tips today are metal coated, pulled single mode optical fibers which were introduced by Betzig et al. in 1991 [16]. These NSOM tips are made by pulling single mode optical fibers while heating the fiber with a CO_2 laser. By controlling the laser power and spot size as well as the pulling force, the fiber tip diameters can be varied from $\leq$50 to $\geq$200 nm, as measured by a scanning electron microscope (SEM). An extensive study of how pulling parameters affect taper angle, final tip size, and optical throughput can be found in [29]. The sub-wavelength apertures are then defined by coating the sides of the tapered fiber with metal. This is usually done with electron beam or thermal evaporation. The tips are tilted up from horizontal by 10–20° and rotated during the coating process. Aluminum is the most commonly used material because it has the smallest penetration depth in the visible and it forms a smooth film. Typical thickness is $\geq$100 nm. Chromium/gold and silver have also been used, but they tend to form islands. Having a smooth metal coating is essential because light can leak out of the tapered fiber between metal islands, i.e. pinholes. When this happens, there is no well-defined aperture or there could be multiple apertures. Furthermore, a grain at the end of the tip can block the aperture and/or prevent the aperture from being close enough to the sample. Cleanliness is another crucial factor in producing pinhole-free coatings. Small debris adhered to the pulled fiber will result in isolated pinholes. Even when there are only one or two pinholes far from the end of the tip, it reduces the output through the sub-wavelength aperture at the end of the taper and produces a background light that degrades the already low signal-to-noise (S/N) ratio in NSOM experiments.

As in other scanning probe microscopies, the quality of NSOM images strongly depends on the tip used in the experiment. Therefore, a careful characterization routine must be in place to examine *every single tip*. In our group, all coated tips are inspected under a high power optical microscope for light leakage through pinholes. Only tips without pinholes are used for experiments. Since the pulling process produces twin tips, the short side of each pair is examined using an SEM to obtain taper end diameters and to make sure that there are no anomalies in the tapering region. Selected tips are also SEMed after Al deposition to examine the smoothness of the Al coating and to measure actual aperture diameter. We found that Al deposition conditions can be optimized so that the end of the fiber is not obstructed by the metal, and the aperture size agrees well with the diameter measured on the uncoated twin tip. Fig. 2 shows SEM images of (a) an uncoated tapered fiber tip in profile and (b) the twin tip after Al deposition, taken head-on [30]. The subwavelength aperture is clearly visible and unobstructed by the Al coating. We then measure the throughput and, for tips used in polarization experiments, check the extinction ratio. Typical tips with 100–150 nm apertures have optical output of 5–50 nW. Only tips with an extinction ratio >100:1 are used when polarization is of concern.

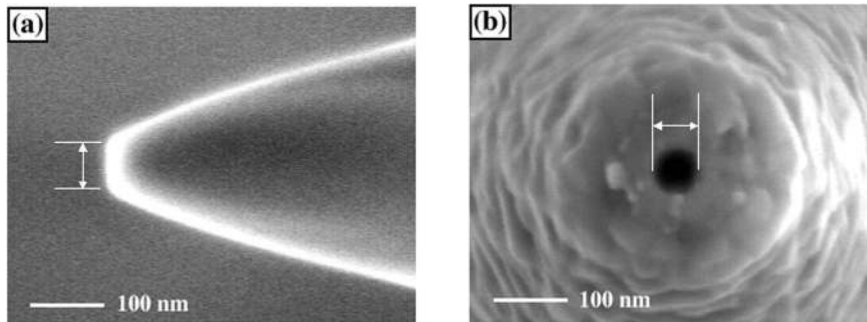

Fig. 2. Scanning electron microscope (SEM) micrographs of tapered optical fiber tips. The two tips shown here are made from one pull, i.e. twins. (a) Side view of an uncoated tip, and (b) a head-on view of its twin coated with aluminum. The sub-wavelength aperture is the dark circle in (b). The flat end of the uncoated tip and the aperture of the coated tip are marked in (a) and (b), respectively. Both measure 61 ± 3 nm, indicating that the aluminum coating is not covering the end of the silica fiber face. [30].

As seen in Fig. 2, the Al coating shows granular structures. The dependence of this roughness on evaporation conditions has been thoroughly investigated and reported in [31]. Even when Al does not obstruct the aperture, protrusion(s) at the end of tip can limit how close the tip can approach the sample. This undesirable effect degrades image resolution as well as polarization extinction ratio. Recently, a focused ion beam (FIB) technique has been applied to "clean" off the Al at the end of the tip [32,33]. This produces tips with very flat and smooth ends, as shown in Fig. 3. The fluorescent count rate of single molecules obtained with a FIB modified tip is an order of magnitude higher than that obtained with an unmodified tip [33]. Hence, this additional step appears to be very promising. However, it adds another step into the already time- and labor-intensive tip fabrication process.

While these pulled fiber tips are significantly brighter than the pulled pipette tips of the previous generation, the throughput is still only 10^{-5} to 10^{-6} of the input light intensity. Another weakness of these tips is the Al coating. Since the mode diameter is significantly larger than the final tip size, much of the optical intensity is not confined in the fiber near the end of the taper. The tapering process also introduces additional scattering. Hence, a significant amount of the power is absorbed by the Al coating and causes heating [34]. Experimental measurements showed that the Al coating near the NSOM aperture can reach temperatures as high as 470°C in operating conditions [35]. Therefore, we cannot arbitrarily increase the input laser power in order to boost the output power at the NSOM aperture. We found, with optimal coupling, a safe working input power is 0.5–1 mW. Significantly above this level, the Al at the end of the tip melts, causing the tip to catastrophically

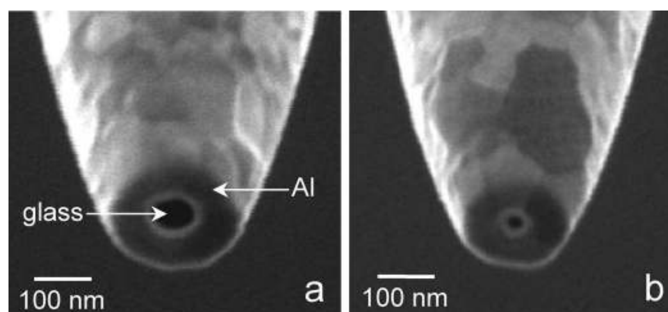

Fig. 3. SEM images of two NSOM probes in which the ends have been milled flat using a FIB. The aperture diameters are (a) 120 nm, and (b) 35 nm [33].

fail. Furthermore, due to the mechanical softness of Al, scanning on a rough surface can sometimes cause tip damage by knocking off a piece of Al. Using an adhesion layer of Ti, Cr, Co, or Ni has been shown to improve the metal coating damage threshold [36].

To achieve higher resolution, smaller apertures with high throughput are necessary. To this end, chemically etched fiber tips were explored [37–40]. In the pulling process, the fiber core is reduced proportionally as the overall diameter is reduced. In contrast, the fiber cores of chemically etched tips remain their original size much closer to the aperture. It is believed that these tips can deliver and collect more light for the same aperture size. Video rate NSOM imaging has been demonstrated [41]. However, getting a smooth metal coating on etched tips turns out to be less reliable than on the pulled tips. FIB modification will be particularly useful for tips fabricated by etching. The batch fabrication method used to produce SFM tips has also been exploited for fabrication of NSOM tips [42–44]. Similarly, transmission through SiN SFM tips has also been tried [45,46]. However, the throughput and reliability of these tips are inferior to fiber tips. Some of the more exotic ''tips'' that have been tried include trapped or attached metal particles [47–49], localized plasmon resonance probe [50–52], attaching a fluorescent molecule at the end of a regular NSOM tip [53], transferring fluorescent energy between tip and sample [54], and using a laser diode as the NSOM source directly [55,56]. An extensive review on alternative NSOM probes can be found in [23]. One of the more promising approaches is apertureless NSOM [57]. The high resolution is achived by illuminating a sharp metal tip to enhance the field right beneath the tip [57,58]. Silicon or silicon nitride SFM tips can also be used to convert evanescent fields to propagating light [59]. Apertureless NSOM has been used to study ferroelectric materials successfully [60].

2.2. Shear force feedback

In addition to having a good quality sub-wavelength light source or detector, another requirement to achieve high spatial resolution is that the sample must be placed in the near-field zone of the tip during scanning. For typical apertures of 100 nm in the visible light regime, the tip–sample separation should be $\leq$20 nm. As a rule of thumb, the tip–sample separation should be less than one-third of the aperture size, the experimentally estimated ''collimation'' distance for these apertures. Since most sample surfaces are not smooth to this degree, a feedback mechanism must be used to keep tip–sample separation constant and to prevent tip or sample damage during scanning. For NSOM, a shear force mechanism has been widely adapted to regulate fiber tip–sample separation. The NSOM tip is attached to a piezoelectric element (the dither piezo) and held vertically above the sample surface. These tapered fiber tips are mechanical structures with lateral vibration normal modes of reasonably high quality factor ($Q \sim 30$–100), analogous to a long rod held at one end. By applying a time-dependent ac voltage to the dither piezo at a selected resonant frequency, the fiber tip is set in vibration parallel to the sample surface. As the tip approaches the sample, the amplitude of this dithering motion decreases due to interaction with the sample. The tip–sample separation can then be regulated through a feedback loop by monitoring the changes in the tip dithering motion.

The first two methods for shear-force distance control in NSOM were independently proposed by Betzig et al. [17] and Toledo-Crow et al. [18]. Both methods are based on optical detection and require the use of a second laser and photodetector in addition to what is needed for the NSOM imaging itself. The more widely used method, following [17], works by focusing the feedback laser onto the fiber tip and monitoring the ac component of the scattered light at the dither frequency. A schematic of a commoly adopted optical detection shear forece setup is depicted in Fig. 4 [61]. Although this optical method regulates distance well, the major disadvantage is that while the light from the sub-wavelength NSOM aperture is $\sim$10 nW in power, the feedback laser power is typically

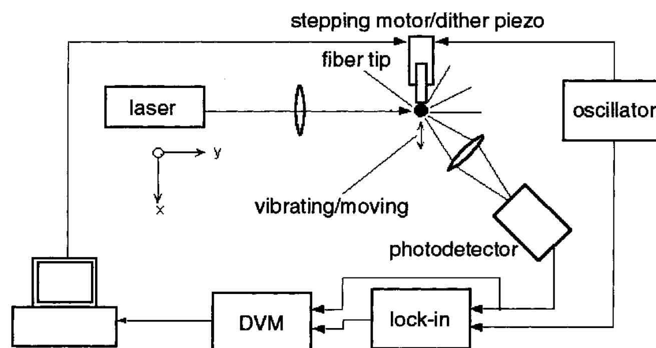

Fig. 4. Schematic of an optical detection shear force setup that is commonly used before the introduction of non-optical detection of shear force. The shear force feedback laser is focused onto the fiber tip, and the ac component of the scattered light at the dither frequency is monitored as the tip is brought near the sample (not shown). The dither amplitude can also be measured using this setup [61].

10^5 times larger, roughly 1 mW. The optical excitations arising from the feedback laser can result in a large background signal and reduce the *S*/*N* ratio for the near-field optical contrast. Through a careful selection of feedback laser wavelength and usage of proper filters, some of these problems can be minimized. However, the feedback laser must then be sample specific. Even worse, optical feedback makes NSOM studies of narrow-bandgap semiconductors (bandgap ≤ 0.5 eV) and superconductors (superconducting gap ≤ 10 meV) impractical. In addition, crucial alignment of the feedback laser, fiber tip, and the photodetector makes it difficult to adapt optical detection methods for operation under non-ambient conditions, e.g. at low temperature or in ultra-high vacuum. Thus, a non-optical method for tip–sample distance control is desirable.

One non-optical method uses the tunneling current from the NSOM tip–metal coating to the sample for feedback control [62], similar to STM. While the tunneling current is extremely sensitive to distance, this feedback method requires the sample to be conducting. This requirement significantly undercuts the power of NSOM, which is an optical microscope and thus can be used to probe near-surface optical properties of any material. Detection of tip–sample capacitance change was also used [63]. A better approach is to monitor the change in the shear force by a non-optical sensing technique. Two methods were introduced in 1995 independently [64,65]. Karrai and Grober proposed mounting the fiber tip on a high Q quartz tuning quark and detecting the amplitude or phase changes of the combined tip/tuning fork resonance, $\sim$33 kHz [65]. This method is the most commonly used NSOM feedback method today. However, there are some drawbacks. The attachment of a fiber tip to the quartz tuning fork is tedious. The tuning fork and the wires near the fiber tip can obscure collection for reflection NSOM imaging. In addition, the *Q* of commonly available quartz tuning forks is high ($\sim$1000), which could limit bandwidth and result in slow scan rates. Several schemes have been shown to overcome the high *Q* limitation and achieve high scan rates [41,66,67]. In our group, we independently developed an approach that does not involve additional elements [64]. The details are given in the next paragraph. Since 1995, many non-optical distance control methods based on variations of these two methods have been introduced.

Our method measures the tip–sample interaction by detecting changes in the electrical impedance of the dither piezo, and to feedback control the tip–sample separation using a signal derived from this impedance change. The basic idea is that a fiber tip attached to a dither piezo forms an electromechanical system with complicated mechanical resonance structures. At a resonance, the system draws more power from the voltage oscillator because of the amplified movement of the

mechanical components (e.g. the tip). The amount of power consumption on resonance is directly proportional to Q, and thus is sensitive to the change in damping force as the tip approaches and interacts with the sample. At the frequencies of interest (30–100 kHz), the change in power consumption is best reflected by a change in the electrical impedance that the dither piezo presents to the oscillator. The dither piezo impedance is mostly capacitive, but becomes slightly more resistive at each mechanical resonance. At a resonant frequency, as the tip nears the surface, the tip–sample interaction causes changes in dither piezo impedance. We observe a decrease in magnitude of impedance ($|Z|$) by a few parts in 10^3 to 10^4 from its value when the tip is far from the sample surface. This change in $|Z|$ is used for tip–sample distance feedback control. Because the change is small, a bridge is used to detect it. An electronic bridge was implemented to replace the simple Wheatstone bridge first used [68]. The use of a lockin amplifier can also be eliminated with high gain current-to-voltage input amplifiers [69]. This non-optical shear force feedback technique can detect topographic height changes <0.1 nm. One drawback of the technique comes from operating the bridge near the balanced point. The signal is very sensitive to slight changes in impedance and to pickups. Temperature changes of the dither piezo and of the electronic components are responsible for most of the signal drift. To minimize drift, the NSOM heads are placed away from any air drafts and encased in Styrofoam boxes if necessary.

In order not to degrade the optical resolution in NSOM imaging, the dither amplitude should be kept well below the aperture size. Direct measurements of dither amplitude reveal that, under typical operating conditions, the tip dithering amplitude far from the surface is several tens of nanometers [61,70]. Since this amplitude is damped when the tip is in feedback, the actual tip dithering motion during imaging is smaller and will not pose a problem in image resolution. This is borne out by experimental observation.

While shear force feedback appears to be practical, the nature of the tip–sample interaction is still under research. Some of the proposed mechanisms are viscous drag, van der Waals force, capillary force, and patch charges. Over the past few years, research has shown two mechanisms are mostly responsible for the so-called shear force. First is a ‘‘knocking’’ mechanism, in which the tip makes intermittent contact with the sample surface [71,72]. The end of the NSOM tip actually bends when it touches the surface. This mechanism is also referred as elastic force [73]. As the tip comes closer to the sample (increasing elastic force), the resonant frequency shifts up, the resonant amplitude decreases, and the resonant peak becomes asymmetric [73,74]. The force also depends on the tilt angle of the tip. If the tip were absolutely perpendicular to the sample, this contribution would be negligible. However, this does not happen in real experiments because surfaces always have topography, the taper might be slightly asymmetric, and it is difficult to mount the tip exactly normal to the sample. When NSOM experiments are in the ambient environment, it has been shown that viscous damping from a condensed fluid-like layer becomes important [75]. The frequency characteristics of viscous damping are reduction in resonance amplitude but no change in resonance frequency. The contribution of this viscous force strongly depends on humidity [76,77]. In general, it has been established that when the tip is ‘‘far’’ away from the sample ($\sim$10 nm) the viscous force dominates, but, when the tip is closer to the surface the elastic force dominates [73,74]. The balance between the two forces depends on tip tilt angle and environment.

When operating in feedback, a topographic image similar to an SFM image is generated based on the z-scan piezo voltage used to maintain a constant tip–sample distance. This topographic image is acquired simultaneously with the optical image. Therefore, NSOM has an advantage over other SFM techniques because both properties are measured at the same sample positions. This eliminates the tedious cross correlation one usually has to do to understand results from two different measurements. One must be cautious of topographic features introducing artificial optical contrast.

This was discussed in details in [78]. On the other hand, the topographic images have been shown to separate true optical properties from topographic induced artifacts [79,80].

2.3. Spectroscopies

As mentioned in Section 1, the power of NSOM lies in the capability to perform local spectroscopic measurements. Photoluminescence (PL) is the easiest to implement and most commonly used spectroscopic tool in NSOM studies. In illumination-mode NSOM PL experiments, light from the NSOM tip is used for excitation and luminescence from the sample at a different energy is collected and analyzed. The availability of sensitive charge couple device (CCD) detectors makes these low light experiments possible. NSOM PL is especially useful for organic and biological studies. It is also used to study semiconductor nanostructures and to differentiate material crystallinity. For example, Grober et al. mapped PL from a single quantum well (QW), multi-quantum wells, and a quantum wire and learned that the broadening in quantum wire PL is due to growth inhomogeneities in the single quantum well (QW) [81]. Also, PL differentiates regions of spontaneously ordered (InGa)P from surrounding disordered materials [82,83]. PL can also be done in collection-mode NSOM. When the excitation wavelength is in the ultraviolet (UV) region, it is necessary to perform a collection experiment because UV light is absorbed by regular fibers. Levy et al. use collection-mode NSOM to study spin dynamics in disordered magnetic II–VI semiconductor heterostructures [84].

Robinson et al. showed that NSOM PL spectra can be very different depending on whether they are taken in illumination or collection mode [85]. Fig. 5 clearly demonstrates this difference. Using the NSOM tip for illumination, the photoexcited excitons can diffuse before they recombine and hence sample different emission sites. All these photons are then collected in the experiment. The spectra are usually broad and similar to far-field spectra. In collection mode, the signal comes only from the excitons that recombine directly underneath the NSOM aperture. Hence, the PL peaks are much narrower and more discrete. The third method is to use the tip both as a source and a collector provided that the excitation light and the PL have different wavelengths or polarization states so that backscattering of the excitation light can be rejected sufficiently. This has been shown to work successfully [86], and in some cases, it produces the best results [87].

Electroluminescence (EL) experiments are similar to PL. In this case, an electrical bias is applied to the sample, a light emitting device. The NSOM tip is used to collect this light. Buratto

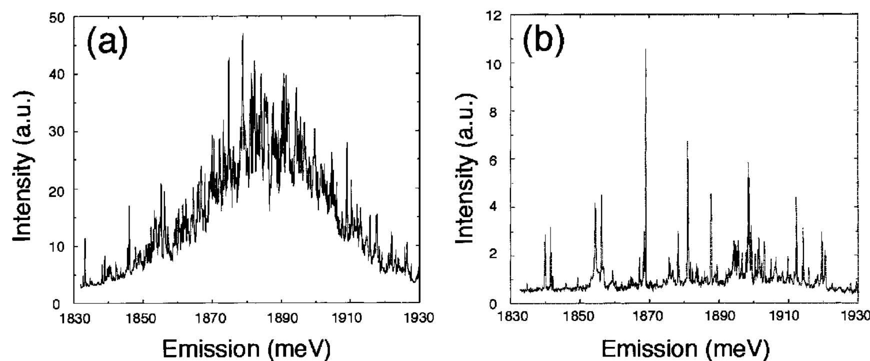

Fig. 5. NSOM PL spectra of InGaAs QDs grown on AlGaAs substrates and capped with a GaAs layer. The spectrum in (a) is taken in illumination mode, and in (b) is taken in collection mode [85].

et al. used this technique to differentiate lasing from active region of a QW laser and EL from the InP substrate [88]. More on this subject will be reviewed in Section 6.1.

In the case of NSOM imaging of single molecules or excitons, the lateral size of the luminescence (spot) is determined by the aperture size since the source of PL is much smaller. While this renders the NSOM not as useful as an imaging tool, it excels as a method to study individual luminescence species instead of the ensemble average. The spatial resolution of PL in semiconductors is much more complicated. It depends on the penetration depth, band bending, surface recombination velocity, and tip size. Numerical studies have shown that the first three are much more important than the tip size. In particular, the resolution is higher for the case where a large surface recombination velocity is combined with a band bending such that the minority carriers drift to the surface [89].

Complimentary to PL is to perform photoluminescence excitation (PLE) experiments, where the wavelength of the excitation light is varied while the luminescence is monitored at a fixed wavelength window. PLE experiments are difficult to do in NSOM because a given single mode fiber works well only in a small wavelength region. The light will propagate in higher order modes for shorter wavelengths, and the transmission drops significantly for longer wavelengths due to bending losses. However, a few groups have successfully shown the usefulness of this spectroscopic mode [90]. Similarly, NPC spectroscopy is done by varying the excitation wavelength. This technique has been used to study defects and aging in high-power semiconductor laser diodes [91]. Herndon et al. performed photocurrent measurements at different wavelengths to map the bandgap variations due to sulfur diffusion in CdTe solar cells [92]. Varying the excitation light wavelength, hence the penetration depth in the semiconductor, provides a means to separate surface and bulk contribution [93].

The availability of picosecond and femtosecond lasers opens up the opportunity to probe photoexcitation dynamics and relaxation. Several groups have coupled time resolved PL with NSOM [94]. Smith et al. first demonstrated that a femtosecond pulse can be sent through an NSOM tip [95]. Levy et al. studied the spatiotemporal dependence of excitonic spin behavior in patterned magnetic heterostructures. They found evidence of spin dependent diffusion being modified by disorders [84,96]. In semiconductors, pump–probe experiments are useful for probing carrier dynamics. The pump light excites carriers in the sample and the probe light monitors changes in transmission or reflectivity. The first pump–probe NSOM experiment was done by La Rosa et al. to investigate recombination of excess carriers in oxidized silicon [97,98]. Vertikov et al. studied heat propagation in patterned gold nanostructures by monitoring the reflectivity changes [99]. Recently, femtosecond pump–probe NSOM experiments were done to probe carrier transport in QWs [100] and quantum wires [101]. In addition, Paulson et al. showed that local photoreflectance spectra across the semiconductor bandgap can be taken using NSOM [102]. Two photon excited fluorescence imaging has been demonstrated with scattering of femtosecond laser light by a metal tip [58].

Raman spectroscopy provides electronic and structural information. Since the cross sections of Raman processes are very small, using NSOM to perform local Raman measurements is extremely difficult. Jancke and Hallen did a tour-de-force experiment to demonstrate NSOM Raman [103]. A single image took 9 h due to the integration time needed to get adequate S/N. This long scanning time puts an extreme demand on the NSOM design [104]. Both thermal and electronic drifts must be eliminated in order to avoid damaging the tip during the several hours of the experiment. They found that the Raman spectra taken at the surface are somewhat different from those taken away from the surface. This can be explained by the z-polarization of the evanescent light [105] that was first demonstrated by Betzig and Chichester on single molecule luminescence [19]. Surface-enhanced Raman imaging of dye molecules has also been demonstrated using NSOM [106,107]. Furthermore, it was shown that using an SFM tip can enhance surface Raman scattering locally [108].

Since infrared (IR) spectroscopy in the molecular vibration wavelength region (400–4000 cm^{-1}, or 2.5–25 μm) provides chemical information, an NSOM operating in this wavelength region will be very valuable. However, normal silica optical fibers do not transmit wavelength longer than 1.55 μm due to absorption. Suitable NSOM apertures can be made by pulling IR transparent fibers, such as fluoride, chalcogenide, sapphire, and low-OH silica fibers [109]. In addition to the difficulty in making bright IR apertures, infrared lasers are less readily available. An IR-NSOM was demonstrated using a free electron laser [110]. High resolution has been shown to be promising for IR-NSOM imaging by the apertureless approach, where a vibrating SFM tip is illuminated from the side by a CO_2 laser [111–113].

2.4. Polarization control

Polarization control of light provides us a tool to study spin dynamics, magneto-optical effects, and optical anisotropy associated with material structures and/or strain. Despite imperfections often found in NSOM tips, a desired polarization state can be generated at the tip with polarized input light and proper control of fiber retardance. For linearly polarized light, an extinction ratio in excess of 2000:1 has been demonstrated [114]. The simplest method is to use an analyzer with its orientation perpendicular to the tip light polarization (crossed polar condition) to analyze the polarization state of the light after passing through the sample. Using light of a known linear polarization and an analyzer before the detector, Faraday rotation was used to image magnetic domains on magneto-optic materials using an NSOM [114,115]. The orientation of a molecular dipole may be determined in single molecule fluorescence imaging with polarization resolved techniques [19]. Linearly polarized NSOM light has also been used to study twin domain structures of lanthanum aluminate [116]. Polarization imaging can aid in distinguishing between genuine optical effects and those arising from large topographic changes [117]. Circular polarization states may be generated as well, making NSOM useful for spin-sensitive measurements [84,96].

One subtle difference between polarization in propagating light, as in conventional optics, and that in the evanescent modes of NSOM is the presence of z-polarization. The direction out of the plane of the aperture is represented by "z". The electric field, hence the polarization direction, in propagating electromagnetic waves must be perpendicular to the propagating direction. This is not the case for non-propagating light. Thus, the electric field right under a NSOM tip has a significant z component as well as the components in the x–y plane. This z-polarization was first seen in the fluorescent images of single molecules [19] and can affect Raman processes, which are sensitive to the electric field direction [105].

The crossed polar technique has several disadvantages. Besides limited sensitivity, two measurements with different sample orientations are required to measure the magnitude and orientation of the sample optical anisotropy. Finding the same region again after sample rotation is difficult and tedious in scanning probe microscopy so it would be advantageous to acquire all of the sample birefringence or dichroism information in one pass. The ability to generate arbitrary elliptical polarization states makes it possible to perform more sensitive polarization modulation experiments, where the ellipticity or polarization direction varies with time. Vaez-Iravani and Toledo-Crow were the first group to successfully combine a dynamic polarimetry technique with NSOM [118]. However, there are a few drawbacks to their technique. The fiber–tip retardance was not compensated and could introduce spurious effects in the results. In addition, spatial variations of sample transmittance contribute to the linear birefringence signals in [118] and can only be taken out using data processing. Moreover, this method did not allow for simultaneous measurement of the magnitude and orientation of the sample birefringence. The orientation of the birefringence must still

be known beforehand. I will describe a polarization modulation NSOM (PM-NSOM) technique developed in our group to measure linear retardance or diattenuation in the sample later [30]. This method resolved the problems associated with the technique introduced by Vaez-Iravani and Toledo-Crow and further advanced PM-NSOM to a quantitative measurement.

In a polarization modulation experiment, a monochromatic beam from a collimated light source is passed first through a linear polarizer oriented at 90°. The 90° polarized beam then passes through a photoelastic modulator (PEM), which is oriented at +45°. The PEM introduces a sinusoidally time varying phase retardance into the +45° polarization component while leaving the −45° component unaffected. Thus, the PEM is effectively a linear retarder with a retardance of $\delta_0 \sin(2\pi ft)$, where δ_0 is the modulation amplitude and ϕ is the modulation frequency (50 kHz) [119,120]. The ellipticity of the emerging polarization state varies at the modulation frequency, and the principal axis remains at 90°. An electrooptic modulator can be used instead of a PEM [121–123]. A quarter wave plate oriented at 0° transforms the elliptically polarized light into linearly polarized light with its orientation varying sinusoidally at the modulation frequency [124]. The sample follows the quarter wave plate. For a birefringent material without dichroism, the linear retardance of the sample introduces a circular component into the previously linear polarized beam. The relative magnitude of the circular component depends on the instantaneous orientation of the incident polarization. Thus, the circular component varies at the modulation frequency and its harmonics. A circular analyzer following the sample transforms this into an intensity variation at the photodetector. The intensity (I) measured by the photodetector consists of a dc term, a term that repeats at odd harmonics, and a term that repeats at even harmonics. Explicitly

$$\begin{aligned} I = I_0\{ & (\tfrac{1}{2} + \tfrac{1}{2} J_0(\delta_0) \sin\phi \sin(2\theta)) + \\ & (-\sin\phi\cos(2\theta))[J_1(\delta_0)\sin(\omega t) + J_3(\delta_0)\sin(3\omega t) + J_5(\delta_0)\sin(5\omega t) + \cdots] + \\ & (\sin\phi\sin(2\theta))[J_2(\delta_0)\cos(2\omega t) + J_4(\delta_0)\cos(4\omega t) + J_6(\delta_0)\cos(6\omega t) + \cdots]\} \end{aligned} \tag{1}$$

where J_n is the nth order Bessel function, ω denotes $2\pi f$, δ_0 represents the amplitude of the PEM modulation, ϕ denotes the magnitude of the phase retardance of the sample, and θ represents the orientation of the optical axis (index ellipsoid) of the sample [125]. By choosing a modulation amplitude of $\delta_0 = 2.405$ (the first zero of J_0), the measurement is simplified because the dc term becomes independent of the sample retardance. The dc term can then be used to normalize the $1f$ and $2f$ signals in order to eliminate the dependence on overall light intensity fluctuations and sample transmittance. Furthermore, it is necessary to collect only the normalized first harmonic ($1f$/dc) and second harmonic ($2f$/dc) to obtain ϕ and θ. Using the optical path described above, these two signals are then

$$\left(\frac{1f}{\mathrm{dc}}\right)_{\mathrm{rms}} = -\sqrt{2} J_1(\delta_0)\sin(\phi)\cos(2\theta) \tag{2}$$

and

$$\left(\frac{2f}{\mathrm{dc}}\right)_{\mathrm{rms}} = \sqrt{2} J_2(\delta_0)\sin(\phi)\sin(2\theta) \tag{3}$$

In this case, $1f$/dc represents the 0°/90° component of linear retardance and $2f$/dc represents the +45°/−45° component. Note that the expressions for the $1f$/dc and $2f$/dc signals were derived with the assumption of no dichroism, and will not hold for samples that are significantly dichroic.

Linear dichroism can be measured in a similar way. Using the same linearly polarized beam with the sinusoidally varying orientation, a sample with linear dichroism will cause the intensity of

the transmitted beam to rise and fall at the modulation frequency and its harmonics. This ac signal can be detected with the circular analyzer removed and the photodetector following the sample. Setting $\delta_0 = 2.405$ and normalizing with the dc component as before, the two components are now

$$\left(\frac{1f}{\mathrm{dc}}\right)_{\mathrm{rms}} = -\sqrt{2}J_1(\delta_0)\left(\frac{p-q}{p+q}\right)\sin(2\theta) \qquad (4)$$

and

$$\left(\frac{2f}{\mathrm{dc}}\right)_{\mathrm{rms}} = -\sqrt{2}J_2(\delta_0)\left(\frac{p-q}{p+q}\right)\cos(2\theta) \qquad (5)$$

where p and q are the intensity transmission coefficients for the two eigen-polarizations of the sample. These two components may be thought of as the $+45°/-45°$ and $0°/90°$ components of linear dichroism. Thus, the diattenuation $(p-q)/(p+q)$ and the orientation of the dichroic axes may be determined from these two signals. The dichroic measurement is valid even if the sample has birefringence, as long as the birefringence orientation is the same as the dichroism orientation. Polarization modulation experiments can also be done with the PEM after the sample [126].

Fig. 6 shows a schematic of our PM-NSOM set up. Light from a 670 nm laser diode passes through a linear polarizer (oriented at 90°), a PEM (oriented at +45°), and a quarter wave plate (oriented at 0°). The PEM is slightly wedged in the plane perpendicular to the propagation direction to prevent interference effects arising from the use of a coherent source. The resulting rotating

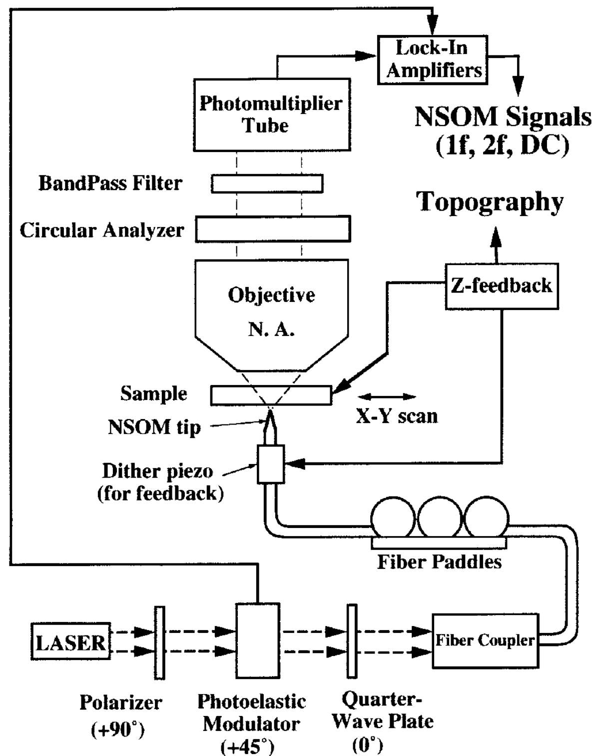

Fig. 6. Schematic of the polarization modulation NSOM experimental setup for measuring linear birefringence (with circular analyzer) or linear dichroism (without circular analyzer) [30].

linearly polarized light is then coupled into a single-mode optical fiber leading to the NSOM tip. The light emitted from the tip aperture and transmitted through the sample is collected by a microscope objective lens. The collected light travels up the microscope column where a circular analyzer may be inserted (birefringence mode) or removed (dichroism mode) before the light reaches a photomultiplier tube (PMT). As the sample is scanned relative to the tip, 1*f*/dc and 2*f*/dc signals are recorded simultaneously for each pixel, building up images. In both birefringence and dichroism modes, the dc component depends only on the local polarization-averaged transmittance of the sample and is used to construct a transmission NSOM image.

Unlike the far-field polarimetry experiment, there are additional optical elements, i.e. the fiber and NSOM tip, between the quarter wave plate and the sample. Care must be taken to minimize the effect coupling anisotropy and tip–fiber retardance has on the PM-NSOM signal. The first effect that must be considered is the anisotropy in the coupling of the light into the fiber. To minimize the unwanted anisotropy, which results in a spurrious dichroism signal, the optical power coupled into the fiber is measured while adjusting the fiber positioning micrometers until maximum coupling efficiency is achieved. With the PEM on, the coupled light then exits the other cleaved end of the optical fiber and is incident on a photodiode (without analyzer). In this arrangement, the difference in coupling efficiency is measured by the experiment as a dichroic signal (see Eqs. (4) and (5)). The micrometers on the launcher are fine-tuned until the 1*f*/dc and 2*f*/dc signals from the photodiode are both zero, thus eliminating the polarization dependence of coupling efficiency. Once this is done, the free end of the cleaved fiber is spliced to the cleaved end of the optical fiber tip.

The retardance of the tip and fiber must also be taken into account. In general, both the magnitude and orientation of the tip–fiber system's retardance will vary depending on the particular tip used, bends in the fiber (causing strain), and the physical path of the fiber. If this tip–fiber retardance is not properly canceled, the ac signals would be a complex function of the tip–fiber system retardance and the sample's retardance. Fiber paddles are used to null out the tip–fiber system's retardance. With the tip in place for the experiment but no sample in, the light from the tip is collected and detected with the PMT. All sections of fiber except the paddles are then fixed in position (taped down), and the circular analyzer is inserted before the PMT. The paddles are adjusted until both the 1*f*/dc and 2*f*/dc signals from the PMT are zero. This procedure cancels the linear retardance of the system (modulo 2π) before the insertion of the sample. These two procedures are necessary to ensure that the retardance measured in the NSOM images is due to the sample and to obtain quantitative results (Section 4.2).

While polarization measurements in the transmission NSOM geometry have progressed substantially, reflection measurements are much harder. The main application in reflection is to use Kerr rotation to study opaque magnetic materials. The main impedance is the loss of polarization information when light is reflected from the sample surface. The metal coating on the NSOM tip poses boundary conditions that must be satisfied for the reflected NSOM light. Recently, a couple groups have demonstrated measuring Kerr rotation using an NSOM [127–129]. Petersen et al. incorporated a Sagnac interferometer into their NSOM tip and measured the rotation of polarization direction of the light reflected back into the tip [129]. The Sagnac interferometer enhances the detection sensitivity for Kerr rotation.

2.5. Low temperature NSOM

Temperature dependence enables us to differentiate different mechanisms and to measure relevant energy scales. For example, activation energy of thermally excited carriers in semiconductors can be obtained. Moreover, quantum phenomena such as electron correlation and

superconductivity can only be studied at low temperatures. Over the past few years, several groups have built low temperature NSOMs (LT-NSOMs) [96,130–133]. Examples of new physics learned with low-temperature NSOMs include spatial and spectral identification of QWs and quantum wires to understand the origin of PL line width [81], localization of excitons by interface fluctuations in QWs [134] and quantum wires [135], and spectroscopies of a single QD to understand carrier relaxation (Section 5.4), to name a few.It is a rich research area in which we will surely see more results in the near future. In this section, we will review the requirements and different approaches in constructing an LT-NSOM.

To date, most LT-NSOMs have used bath cryostats. These demonstrated that the NSOM tips can survive in a liquid helium environment. However, some limitations are associated with cooling the whole microscope. Generally, it requires many hours to reach low temperature, and the scan range is drastically reduced due to the temperature dependence of piezoceramic materials [136]. Furthermore, because of the lack of optical access, these microscopes work best where phenomena of interest can be observed over a large portion of the sample and when a wide range of temperature is not needed. Recently, some groups introduced LT-NSOMs in which only the sample was cooled. This was done through thermal linking to a cold finger via copper braids [137,138]. These microscopes have the advantages of a large low temperature scan range and the ability to change temperature rapidly. Since the size of the NSOM head can be much smaller in these designs, it can be incorporated in a regular optical microscope [138]. Such a design provides the capability to locate a specific sample position at low temperature. It is ideal for studying devices, where the interest of study might be in specific areas of a few microns lateral dimension.

Fig. 7 depicts a schematic representation of the variable-temperature NSOM (VT-NSOM) in [138]. It features a continuous flow cryostat cooled sample stage, a scan area suitable to imaging small devices, high vacuum operating conditions, perpendicular overhead far-field viewing of the scan region, and non-optical feedback. The entire microscope occupies a space smaller than a 3 in.

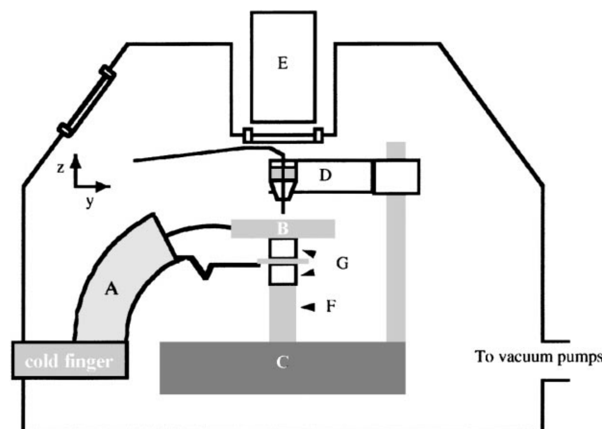

Fig. 7. Schematic representation of the VT-NSOM. The cooling system includes the cryostat cold finger assembly and high thermal conductivity Cu braids (A). The base of the microscope consists of a Cu sample stage (B) and shield attachment, Macor separators (G), a piezo scan tube (F), and the x–y translation stage and motors (C). The Ti head (D) of the microscope includes the tip holder, dither piezo tube and z positioning screws. A recessed cavity in the vacuum chamber allows an external optical microscope objective (E) to be positioned behind the tip. The vacuum chamber has windows mounted directly over the sample stage and on the side at 55° off-vertical. Temperature is controlled and monitored at the cold finger. The temperature is also monitored on the sample stage (B). The head (D) is held firmly to the base (C) by springs. NSOM tips are glued into steel capillary tubes that are held into the tapered mount by set screw. NSOM base and head together fit inside a 3 in. cube [138].

cube. This allows it to be housed inside a vacuum chamber measuring 5 3/4 in. in external diameter with a maximum height of 6 3/8 in.. Both the tip and the sample can be changed with a short turn-around time. The entire temperature range from 12 to 400 K is accessible depending on the balance between heater and cooling power. However, since only the sample is cooled, the lowest achievable temperature is substantially higher ($\sim$12 K) than that in liquid helium bath systems (<4 K). Still, the range is more than adequate for studying semiconductor and high-T_c superconductor systems. The salient feature of this VT-NSOM is that the microscope head was designed to be small enough so that an ex situ conventional optical microscope equipped with a long working distance objective can be used to view the tip position with respect to the sample with $\sim$5 μm accuracy. Since the scan range of the VT-NSOM is 35 μm $\times$ 35 μm below 100 K and larger at higher temperatures, the external viewing allows us to locate the tip on specific sample areas and to reposition the tip to the same sample position after changing temperature. This unique capability was not available in previous bath LT-NSOMs.

A drawback of cooling sample only is condensation on the sample surface because it is substantially colder than the surroundings. In our design, the cold finger of the continuous flow cryostat is the lowest temperature point in the system. During the cool down, the sample temperature is maintained significantly higher than the cold finger to make sure that condensation primarily occurs at the cold finger. With this precaution, the VT-NSOM (typical chamber pressure $\sim 10^{-6}$ Torr before cooling) can be operated at low temperatures for 5–8 h without obvious changes in the topographic images. Even better performance can be achieved by baking out the chamber overnight to lower the starting pressure before cool down.

3. Dislocation electrical activity in relaxed GeSi films

Defect characterization is one of the most important and active fields in materials science and engineering. Because the sizes of most crystalline defects are well below the diffraction limit of visible light, electron microscopy, e.g. transmission electron microscopy (TEM) and EBIC, has been commonly used for this purpose. Since NSOM offers resolution higher than the diffraction limit, it is desirable to use NSOM as an optical method for defect characterization. In addition, NSOM uniquely provides the capability to study surface morphology and electrical activity of the same defect directly and non-destructively.

The presence of dislocations is often detrimental to semiconductor device performance. This is because in addition to the intrinsic defects of the dislocations themselves (e.g. kinks and dangling bonds), dislocations tend to getter point defects and impurities. In many, if not most, materials, electrically active defects, e.g. recombination centers or traps, which affect carrier transport, are associated with dislocations. They can also act as unwanted current leakage paths in electronic devices. Structural properties of dislocations are best characterized by TEM. However, TEM cannot provide information on how dislocations change the physical properties of the materials, e.g. how effective a recombination center a particular type of dislocation is. EBIC is often used for this purpose. EBIC signal is reduced near electrically active defects. The strength of defect electrical activity can be obtained from EBIC contrast. Due to the generation volume of the electron beam, typical EBIC resolution is 1 μm. Similar spatial resolution can be achieved in photocurrent experiments with focused light. Since the NSOM aperture size is 100 nm, a ten-fold increase in spatial resolution can be expected. This section will review NSOM works done on studying the electrical activities of dislocations in relaxed GeSi films [139–141]. The NPC technique is reviewed in Section 3.2. This technique is useful for probing optoelectronic properties and has been applied to

investigate various materials and devices. The question of what physical parameters determine the resolution in NSOM defect imaging is addressed in Section 3.3 [142]. Studying temperature dependence helps shed light on the physical origin of electrical activities in dislocations [143]. Some on-going work on how dislocation strain fields might alter local electronic properties is summarized in Section 3.5.

3.1. Compositionally graded, strain-relaxed GeSi films grown on Si substrates

Relaxed GeSi films have been used to fabricate Si (Ge) heterojunctions with high two-dimensional (2D) electron (hole) gas mobility [144–146], and to integrate GaAs and InGaP light emitting diodes on Si [147]. Thus, the growth of good quality films having bulk properties on lattice mismatched substrates and the characterization of such films have been a major area of study in materials science. Growth details and physical properties of the samples studied here were reported in [147–149]. They were grown by molecular beam epitaxy at temperatures of 800–900°C. The structure consists of a uniform $Ge_{0.3}Si_{0.7}$ cap layer of $\sim$1 μm on top of a compositionally graded layer on Si (0 0 1) substrate with a 100 nm buffer layer. The grading rate was typically 10% Ge per μm. The films are completely strain relaxed, exhibiting bulk $Ge_{0.3}Si_{0.7}$ optical properties. The samples have been extensively characterized [147–150] by X-ray, Rutherford backscattering, TEM, EBIC, and SFM to determine the degree of relaxation, composition, misfit dislocation network structure, threading dislocation densities, and surface roughness. Typically, these graded films have threading dislocation densities between 1×10^5 and 5×10^6 cm^{-2}. This was determined with EBIC because the density is too low to be detected by TEM.

SFM topographic images show two distinct features on the surfaces of these compositionally graded, strain-relaxed GeSi samples: non-periodic surface undulations (peak to valley <300 Å) running along $\langle 110 \rangle$ directions, commonly called crosshatch patterns, and shallow depressions of $\leq$20 nm in depth and 250–500 nm in diameter [150]. The latter were first identified as threading dislocations based on the excellent agreement on many samples between the pit densities seen in SFM images and the threading dislocation densities determined by EBIC. However, it was difficult to perform the EBIC and SFM experiments on the exact same sample positions. Using NSOM to perform local photoresponse measurements while also taking surface topographic images provides a way to show that these surface depressions are truly electrically active threading dislocations without relying on cross correlation. SEM is not sufficiently sensitive to detect these shallow depressions because both height and chemical content change very little. NSOM provides the unique tool for this experiment: it is sensitive to changes in surface topography, similar to SFM, and, at the same time, the spatially resolved photoresponse provides electrical information analogous to EBIC.

3.2. Near-field photocurrent (NPC) experiment

In the NPC experiment, the GeSi samples are photoexcited by light from the NSOM tips and the spatial variation of the photoresponse is measured. The samples have built-in p–i–n junctions parallel to the film surface (Fig. 8). Upon absorption of a photon, a photoresponse signal in the form of a short circuit current (photocurrent) or an open-circuit voltage (photovoltage) is generated in the external circuit. Fig. 9 shows how NPC signal and the shear force signal (open loop) depends on tip–sample separation. NPC signal increases rapidly in the near-field and becomes saturated when the tip is in contact with the sample. Typically, images were taken with tip–sample separation of $\leq$10 nm. The spatially resolved photoresponse was collected simultaneously with the topography of the samples, producing topographic and photocurrent/photovoltage images at the same sample region.

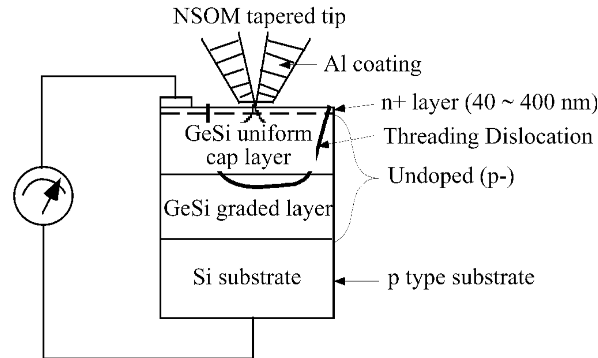

Fig. 8. Schematic diagram (not to scale) of the GeSi/Si sample cross section and the NPC experimental geometry [140].

The topographic information was obtained automatically because we were regulating the tip–sample separation. The laser source for the experiment was a diode laser with 670 nm wavelength. The laser light was chopped at 1 kHz before being coupled into the fiber tip, and the NPC signal was detected using a lock-in amplifier. NPC signal was measured without external bias. Detecting photovoltage at zero bias produces similar images.

In addition to the example shown here, NPC imaging is very useful to locate the exact position of p–n junctions. Due to the built-in electric field, the signal is largest when photoexcitation occurs in the depletion region. Minority diffusion length can be obtained from fitting the decay length away from the junction [151–153]. In laser diodes, it is important to know whether the blocking layers are working properly [151]. In solar cells, whether it is a hetero- or homo-junction [154] and understanding where light is absorbed [92,93] are critical to device efficiency.

3.3. Room temperature results

Fig. 10 shows 5.5 μm × 5.5 μm (a) topographic and (b) NPC images taken on a GeSi sample showing a dislocation pileup along a ⟨1 1 0⟩ direction. Dark spots in the NPC image (Fig. 10(b)) indicate regions of fast carrier recombination, i.e. electrically active defects. The strength of the defect electrical activity is reflected in the magnitude of NPC signal reduction. Because a topographic image is taken at the same sample position, a comparison can be made to differentiate among various types of defects. The isolated dark spots with contrast of 8–10% in Fig. 10(b) are

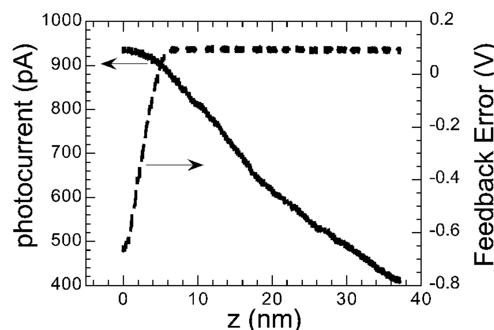

Fig. 9. Near-field photocurrent (NPC) signal and shear force feedback error signal (open loop) vs. tip–sample separation [161].

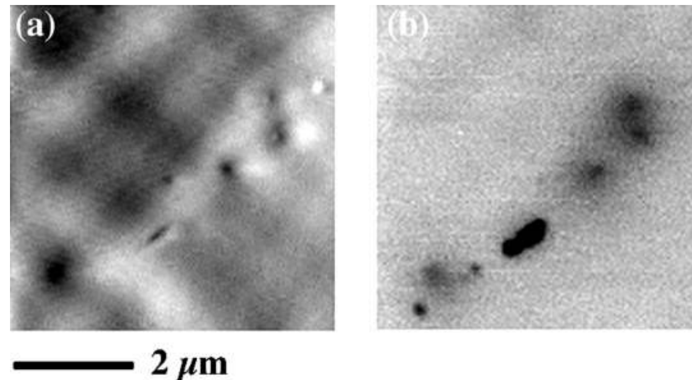

Fig. 10. (a) Topographic and (b) NPC images (5.5 μm × 5.5 μm) of a compositionally-graded, strain-relaxed GeSi film grown on (0 0 1) Si substrate, showing a dislocation pileup. The two dark spots at the lower left corner of the NPC images show no corresponding topographic changes. Their lateral sizes are ~100 nm; hence, they cannot be imaged with EBIC or far-field photocurrent measurements. [28].

commonly seen in these relaxed GeSi films. They have a corresponding shallow depression on the surface. Based on their surface topography and density, we believe they are individual 60° dislocations, the most common type of threading dislocations in these samples. The very dark elliptical shape in the middle of Fig. 10(b) has a contrast over 30% and is highly unusual. When the grayscale is adjusted, we can see that this defect consists of two close-by defects with large contrast. The very different electrical activity indicates that these are different types of dislocations or they have incorporated impurities. Note the two dark spots on the lower left corner of Fig. 10(b). Their diameters are ~100 nm and cannot be imaged with EBIC or conventional far-field photocurrent techniques. Furthermore, they have no corresponding topographic features, indicating that they are likely to be sub-surface defects. A sub-surface electrically active defect displays no topographic change, but shows a reduction in photoresponse when the tip is directly over it [140,141]. Because they are farther from the NSOM aperture, sub-surface defects in NPC images generally appear to have less resolution than the surface defects. The signal and resolution in EBIC measurements depends strongly on the p–n junction bias, whereas in NSOM, bias changes the total NPC signal strength, but does not affect contrast and resolution strongly [141]. This suggests that NPC measurements are more surface sensitive than EBIC.

3.4. Resolution and contrast in NPC defect imaging

With the demonstration of high resolution in NPC defect imaging, it is important to understand what physical parameters determine the resolution and contrast and what sample properties can be extracted from the images. The resolution in NPC images, as well as in EBIC images, depends on the size of the carrier generation volume and the carrier diffusion length. To achieve quantitative understanding, we introduced a 2D model taking into account carrier diffusion and non-uniform excitation [142]. The results show that the apparent defect size, i.e. the width of the reduced photoresponse region, in the NPC images is determined by the NSOM tip aperture size rather than by the carrier diffusion length, as previously believed. Therefore, two defects separated by a distance larger than the aperture size but smaller than the diffusion length will be resolved in NPC imaging. For many materials, defect separation is often larger than the size of the probe and smaller than the diffusion length. The nanometer resolution in NPC imaging results from both the reduction in carrier lifetime near the defects and the reduction in excitation volume.

In the NPC experiment, the steady-state carrier density is given by

$$\frac{\partial n(\vec{r})}{\partial t} = D\nabla^2 n(\vec{r}) - \frac{n(\vec{r})}{\tau(\vec{r})} + S(\vec{r}) = 0 \qquad (6)$$

where $n(\vec{r})$ denotes the carrier density, D is the diffusion constant, $\tau(\vec{r})$ represents the carrier lifetime that has spatial dependence near defects, and $S(\vec{r})$ is a position-dependent source term due to the NSOM light. The NSOM light is taken to be a 2D delta function, $S(\vec{r}) = S_0 R^2 \delta(\vec{r} - \vec{r}_0)$, where R is the radius of the NSOM aperture and $\vec{r}_0$ is the position of the light source. The lifetime is assumed to change abruptly at the defect, i.e.

$$\frac{1}{\tau(\vec{r})} = \frac{1}{\tau_0} + \frac{b^2}{\tau_1}\delta(\vec{r}) \qquad (7)$$

where τ_0 represents the carrier lifetime in the defect-free region, τ_1 is the carrier lifetime inside the defect, the defect physical size is denoted by b and is located at the origin. The defect size is assumed to be smaller than R and diffusion lengths ($l_0 = \sqrt{D\tau_0}$, and $l_1 = \sqrt{D\tau_1}$). Eq. (6) in 2D can be solved analytically as well as numerically [142]. Since the photocurrent experiment measures total carriers collected and not carrier densities, we must integrate $n(\vec{r}, \vec{r}_0)$ to obtain $N(\vec{r}_0)$, the total carriers generated when the NSOM probe is located at $\vec{r}_0$. An image analogous to the NPC image is formed by plotting N as the probe is moved with respect to the defect.

An image of $N(\vec{r}_0)$ in vicinity of two closenear-by defects is shown in Fig. 11(a). The line cut across the two defects is shown in Fig. 11(b). The defects are modeled as two delta functions with radii $b = 10$ nm and separated by 0.5 μm. The radius of the photoexcitation (NSOM light) is assumed to be 50 nm and the intensity is taken to be 1 nW. We used 32 μm as the diffusion length ($\tau_0 = 1$ μs and $D = 10$ cm^2/s) in the defect-free region and $l_1 = 32$ nm within the defects. It is clear from Fig. 11 that the two defects are well resolved even though the bulk diffusion length is orders of magnitude larger. Varying the carrier lifetime in the defect-free region changes the overall signal but has little effect on the defect size in the image. Increasing the carrier lifetime within the defects, however, dramatically reduces the defect contrast.

Fig. 12(a) depicts a typical NPC image of a threading dislocation. The dots in Fig. 12(b) are the line cut through the defect as shown in Fig. 12(a). This NPC image was taken using a tip with aperture size $2R = 140$ nm, as measured by SEM. The line cut through this defect image shows a

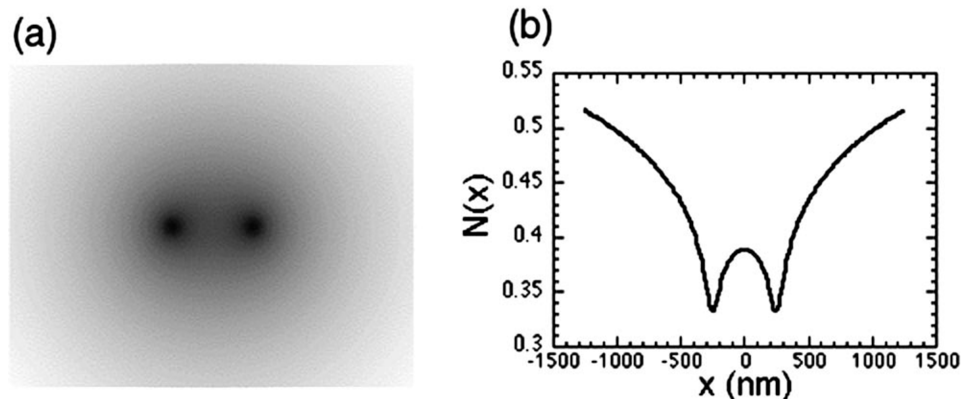

Fig. 11. (a) Numerically calculated image of two nearby defects separated by a distance 0.5 μm. $D = 10$ cm^2/s, $l_0 = 32$ μm, $l_1 = 32$ nm, $R = 50$ nm, and $b = 10$ nm; (b) line cut through the defects [142].

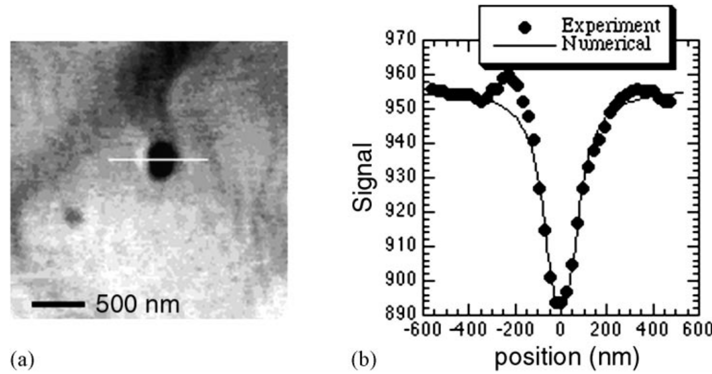

Fig. 12. (a) An experimental NPC image of a threading dislocation; (b) a line cut (●) across the defect as marked in (a) and the theoretical result (solid line) generated using $l_0 = 300$ nm, $l_1 = 100$ nm, $R = 70$ nm, and $a = 10$ nm. The NPC image was acquired using an NSOM and the tip aperture size $2R = 140$ nm [142].

photocurrent reduction region centered at the defect. The size of this depression is approximately equal to the NSOM tip aperture size. In the 2D numerical simulation (solid line in Fig. 12(b)), we fix the parameters $D = 3$ cm^2/s, $R = 70$ nm, $b = 10$ nm, and $\tau_0 = 300$ ps (or $l_0 = 300$ nm), and vary τ_1 (or l_1) until the $N(\vec{r}_0)$ line cut has the same contrast as the experimental data. The theoretical result best matched the experimental data is for $\tau_1 = 33$ ps (or $l_1 = 100$ nm). S_0 is not important in our simulation since we are only interested in matching the shape of the line cut. The signal enhancement to the left of the defect in the experimental data (Fig. 12(a)) is reproducible, indicating that the dislocation defect has a more complex electrical activity structure than what is assumed in Eq. (7).

In general, spatially-averaged τ_0 can be measured using an independent method, D can be determined through mobility measurements, and the NSOM tip aperture size can be obtained through SEM. The fitting of theoretical results to experimental data is then reduced to a one-parameter fit, namely τ_1. Therefore, the carrier lifetime inside a single isolated defect can be obtained from NSOM images. The lifetime associated with an individual defect obviously cannot be obtained from spatially averaged measurements. Due to the various roles of carrier diffusion, carrier collection, and finite excitation size, detailed numerical modeling is needed to extract quantitative information from experimental NPC data.

Thus, the resolution in NPC defect imaging is determined largely by the tip size. Donolato reached the same conclusion for EBIC imaging of dislocations [155,156]. This conclusion might seem a bit surprising to some readers since it is commonly thought that diffusion length determines the imaging resolution. Indeed, NSOM imaging across a p–n junction produces NPC peaks with width significantly larger than the aperture size. This width is due to minority carrier diffusion [152]. The reason that diffusion length determines the resolution in imaging a p–n junction is because there is no reduction in carrier lifetime across the junction, i.e. no defects. The carriers can move a great distance in the built-in field. In the case of defect imaging, if the defect electrical activity is very strong, the carriers basically disappear when they reach the defect. In this case, the resolution is determined by the larger of the excitation size or the defect size. Moreover, surface recombination has a large effect on imaging across a p–n junction [91].

3.5. Temperature dependence

Studying the temperature dependence of the dislocation photoresponse helps shed light on the physical origin of its electrical activity because carrier lifetime depends on the position of defect

states in the bandgap. Our group measured the temperature dependence of photocurrent response associated with individual threading dislocations and with the misfit dislocation network over the range 300–12 K [143]. Studying the same defect as a function of temperature eliminates the ambiguity arising from a distribution of recombination strengths among different defects. This is critical for drawing conclusions when the temperature dependence is weak.

The VT-NSOM described in Section 2.5 [138] was used in this experiment. NSOM experiments are performed at fixed temperatures after the temperature, monitored at the sample stage, has stabilized. Fig. 13(a)–(d) show the simultaneously taken topographic and NPC images of the same five threading dislocations at room temperature and at 48 K. The *S*/*N* is better at low temperatures because the overall photoresponse is larger. This is due to the increase in mobility as temperature decreases [157]. The NPC contrast, expressed in percentage change, is defined as the reduction in the signal at the defects normalized by the NPC signal at a nearby defect-free region. The NPC images,

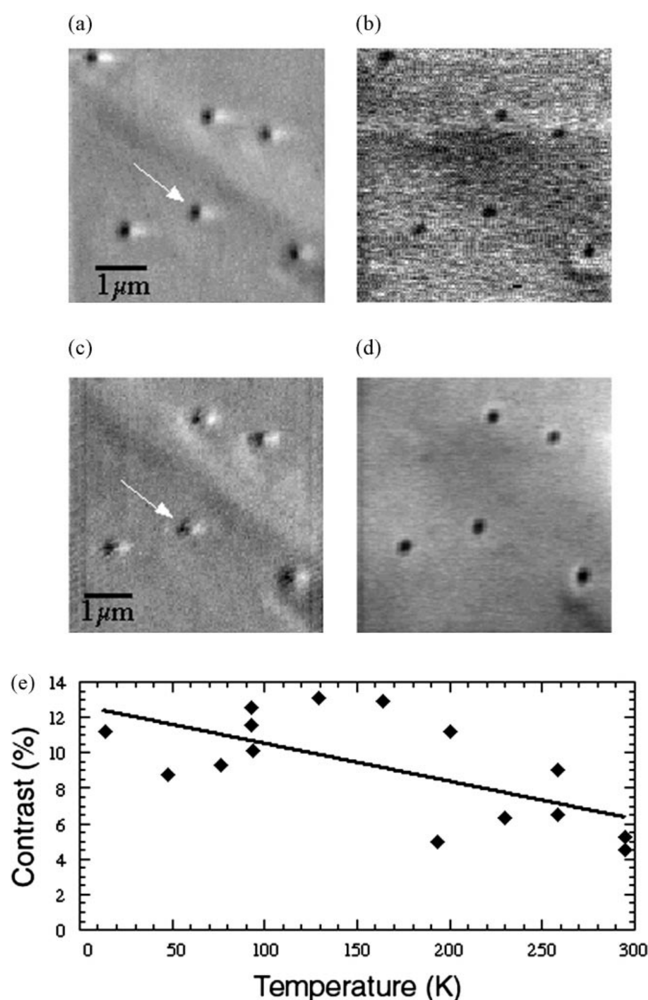

Fig. 13. Simultaneously acquired (a) topographic, and (b) NPC images (5.5 μm × 5.5 μm) of five threading dislocations at 297 K. The same area (5 μm × 5 μm) re-imaged at 48 K; (c) topographic and (d) NPC images. The gray scales are 6 nm, 5% contrast, 5.4 nm, and 10% contrast for (a), (b), (c), and (d), respectively. (e) NPC contrast as a function of temperature for the defect labeled by the arrows in (a) and (c). Different points at the same temperature represent data taken at different runs [143].

hence the percent contrast for a given defect, are acquired at different temperatures. Fig. 13(e) depicts the NPC contrast as a function of temperature from 13 to 297 K for the defect labeled in Fig. 13(a) and (c). We observe a slight increase in the dislocation contrast (larger signal reduction at the dislocations) as temperature decreases. All dislocations in this sample follow this general trend. The temperature dependence of defect contrast reflects how the difference between τ_1 and τ_0 changes with temperature. Based on Shockley–Read–Hall recombination statistics, τ due to shallow centers decreases as temperature decreases while deep centers show the opposite trend [158,159]. Thus, the NPC contrast should increase at low temperatures (a negative temperature coefficient) for shallow center defects. Therefore, our results indicate that the states associated with 60° threading dislocations in these GeSi films are shallow. EBIC studies of misfit dislocation contrast in intentionally Cu contaminated GeSi samples attribute shallow centers to intrinsic defects or low levels (ppb) of contaminants while deep centers are associated with impurity precipitates [160]. In particular, dislocation elastic strain fields are believed to have shallow states. Thus, the weak room temperature contrast and a negative temperature coefficient observed for dislocations in these relaxed GeSi films indicate that the electrical activity of these dislocations is governed by shallow centers, due to either intrinsic defects or low levels of contaminants.

3.6. Mapping strain field distribution using linearly polarized light

As seen in Fig. 12, regions of enhanced NPC signal near threading dislocations were sometimes observed. Furthermore, the crosshatch patterns show a weak contrast in both EBIC and NPC imaging, the origin of which is currently not well understood. Recently, polarized NPC experiments were performed on these samples [161]. In this experiment, NPC images at the same sample position were taken using linearly polarized NSOM light at orthogonal orientations. Fig. 14 shows the results of polarized NPC images near a threading dislocation: (a) topographic, (b) and (c) NPC images taken with linearly polarized light oriented at -45° and $+45^{\circ}$, respectively, (d) NPC image taken with light containing equal $\pm 45^{\circ}$ linear polarization components, and (e) is an average of (b) and (c). It is clear from Fig. 14(b)–(d) that the dark spot that corresponds to shorter carrier lifetime in the dislocation does not change with polarization direction. However, the bright spots are observed along the polarization directions only. Since the orientation of the polarization axis is the only change between Fig. 14(b) and (c), the differences in the two NPC images cannot be the result of a topographic effect, or of carrier diffusion and/or recombination. The similarity between Fig. 14(d) and (e) clearly shows that the NPC enhancement is controlled by the polarization direction of the excitation light. Anisotropic absorption is the most likely explanation for the observed polarization dependence, and is currently under investigation.

Similarly, polarization dependence was observed for the crosshatch contrast. The origin of crosshatch contrast in NPC and EBIC is still not understood. Originally, it was thought to arise from junction depth variations due to the undulating morphology. However, contrast variations due to junction depth would not depend on the polarization direction. Another consideration in the NPC results comes from the difference in absorption (reflection) coefficient for s- and p-polarized light. For the measured slope of the crosshatch undulations, this effect would produce a contrast that is an order of magnitude smaller than the experimentally observed value. The most probable explanation for the crosshatch contrast is strain-induced birefringence and/or dichroism [162]. Strain fields associated with dislocations are not isotropic. They can cause variations in local band structure. For example, anisotropic strain in orthogonal [119,120] directions can split the L valley degeneracies. Hence, the absorption coefficient depends on the crystallographic direction. Higher absorption, and hence larger photocurrent signal, is expected when the excitation polarization is parallel to directions with lower L valleys.

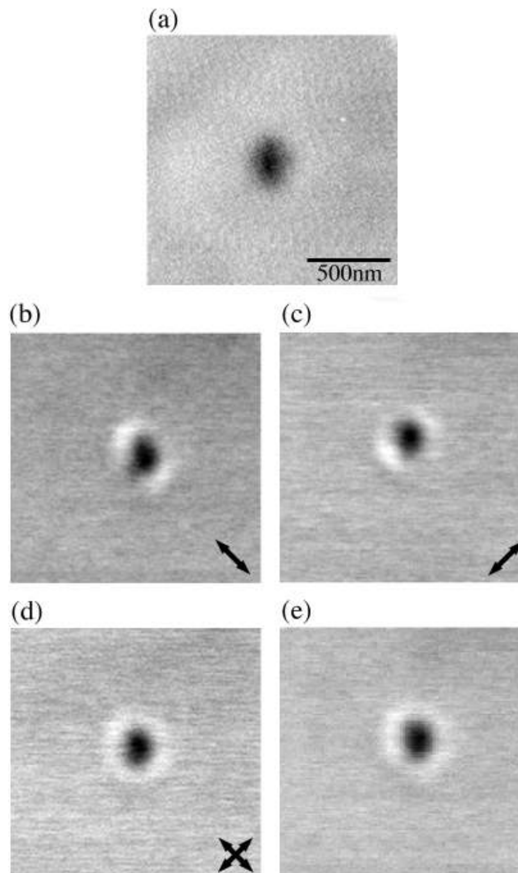

Fig. 14. Near-field photocurrent (NPC) images of a threading dislocation in a relaxed GeSi film taken with linearly polarized light: (a) topography; (b) NPC image with linear polarization direction at −45°; (c) NPC image with linear polarization direction at +45°; (d) NPC images with equal weight of +45° and −45° linearly polarized light; (e) numerical sum of (b) and (c) [161].

The stress tensor for the relaxed GeSi structure was calculated numerically [163]. The misfit dislocations were assumed to nucleate randomly. From the stress tensor and deformation potential for Ge, the change in L valley position was obtained. Taking this as the band gap in different directions, a directional absorption coefficient was calculated. The polarized NPC signal is related to the absorption coefficient difference. Similarly, stress changes the refractive index anisotropically and can be calculated the same way. Both numerical calculation and experimental results show a symmetric (polarization independent) and an asymmetric (polarization dependent) component. The numerical calculation produces contrast of the same order of magnitude as the experimental results. Hence, strain-induced birefringence and/or dichroism is most likely to be the origin of the apparent crosshatch electrical activity.

4. Microstructural defects at oxide bicrystal boundaries

Josephson junctions are the building blocks of superconducting electronics, similar to p–n junctions in semiconducting electronics. A principal challenge in the development of HTSC Josephson junctions as a viable technology lies in reproducibly fabricating junctions with predictable critical current I_c and finite-voltage resistance R. One method commonly used to fabricate HTSC

Josephson junctions is by growing a HTSC film on a bicrystal substrate formed by fusing two single crystals with misaligned crystal axes. Josephson weak links are formed at the grain boundary in the HTSC film grown over the substrate fusion boundary. Despite the wide use of bicrystal substrates, GBJJs fabricated by this method often exhibit drastically different transport characteristics, even on the same substrates. TEM work on the substrate bicrystals showed that the fusion boundary was straight to within 3 nm, but also revealed the presence of voids bounded by {1 0 0} and {1 1 0} planes [164–166]. The HTSC grain boundary follows the fusion boundary line on average, but can wander significantly [164–167]. Transport properties of GBJJs have been studied extensively [168,169], but the influence of such boundary defects on junction transport has not been thoroughly investigated. To advance HTSC electronics requires a detailed understanding of the main causes of junction current inhomogeneity. In particular, it would be most useful to understand thoroughly the relationship between the structural properties of the junction weak link and the electrical quality of the device. To this end, combining NSOM studies with superconducting transport measurements on $YBa_2Cu_3O_7$ (YBCO) GBJJs has shed some light on the origin of device non-uniformity [170–174]. Sections 4.1–4.3 of the review will summarize these results.

4.1. Transmission studies of oxide bicrystal substrates

The substrate bicrystals consist of two pieces of (0 0 1) single crystals fused together with a relative misalignment of the in-plane crystallographic axes. Fig. 15 depicts a diagram of a bicrystal with a 24° symmetric tilt boundary. The angle refers to the total angle made by the $\langle 1\,0\,0 \rangle$ axes of the two single crystals. In another word, one single crystal is rotated 12° clockwise with respect to the fusion boundary about the (0 0 1) axis while the other is rotated 12° counterclockwise. The misalignments (tilt angles) of all the bicrystals studied are symmetric. As for almost all YBCO GBJJs to date, these bicrystals come from Nikko Hitech Inc., with dimensions of $1\,\mathrm{cm} \times 1\,\mathrm{cm} \times 0.05\,\mathrm{cm}$. Since these substrates are polished to a root mean square (rms) roughness of 1 Å, SFM yields little information about defects. However, regions of inhomogeneous refractive index refract light and cause contrast in optical transmission images. To achieve the submicron resolution necessary for detecting microstructural defects, transmission NSOM experiments were done.

Fig. 16 shows an example of (a) NSOM transmission and (b) topographic images taken on a 24° $SrTiO_3$ bicrystal. It is clear that the topographic image cannot tell us the location or the quality of the fusion boundary. However, it is very easy to identify the fusion boundary from the transmission image. The optical transmission along the fusion boundary is not uniform. Instead, circular dark

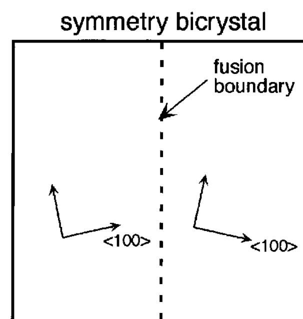

Fig. 15. Diagram of a bicrystal with a 24° symmetric tilt boundary. The angle refers to the total angle made by the $\langle 100 \rangle$ axes of the two single crystals. In other words, one single crystal is rotated 12° clockwise with respect to the fusion boundary about the (0 0 1) axis while the other one is rotated 12° counterclockwise.

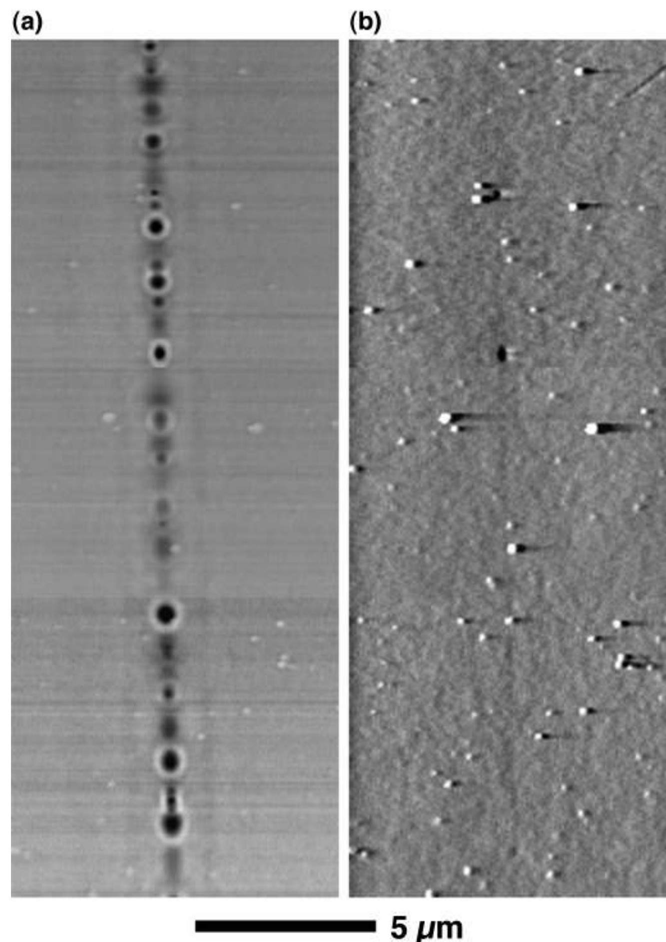

Fig. 16. (a) NSOM transmission, (b) topographic images taken on a 24° $SrTiO_3$ bicrystal [173].

spots with diameters ranging from 0.1 to 1 μm are observed along the boundary. Careful examination of the topographic image reveals that some dark spots have a pit associated with them. However, the majority of them are only seen in the optical image. These defects are found only at the boundary and the reduction in the transmitted intensity is due to light scattered out of the optical collection path [175]. The optical contrast, defined as the reduction in transmission intensity at the defect normalized by the transmission intensity away from the boundary, of these defects varies widely, from 1.5 to 67% [173]. The defect distribution is inhomogeneous over length scales of a few microns along the boundary line; there are regions of several microns long over which there are no observable defects. We believe that these optical dark spots are likely due to the voids reported in TEM studies [164–166] although we cannot definitively rule out the possibility of them being second phase precipitates. The presence of pits associated with some dark spots and the dependence of their optical contrast on wavelength [173,176] strongly argue that they are regions of low refractive index. Based on the fact that these defects were not resolved when an image was taken at the same sample position but with the tip withdrawn about one wavelength from the sample surface, we conclude that they are within a wavelength of the sample surface [171].

While the images in Fig. 16 were taken on a 24° $SrTiO_3$ bicrystal, they exemplify the optical transmission across fusion boundaries of all bicrystals regardless of materials or boundary tilt angle,

with only quantitative variations [172]. Hence, these defects are most likely extrinsic, process-related, and not intrinsic to bicrystals. For example, the defect density and contrast observed in 36° $SrTiO_3$ bicrystals depended strongly on when they were made. The bicrystals from an older batch contain significantly more defects. To confirm the extrinsic nature of these defects, a 0° $SrTiO_3$ bicrystal was studied for comparison. The defect density in this bicrystal is extremely high, similar to the old 36° $SrTiO_3$ bicrystal. Since there is no misorientation between the two single crystals across the fusion boundary, there should not exist any intrinsic defects such as dislocations. Thus, all defects in this sample must be extrinsic and are introduced by the process of cutting the original crystal in half and fusing the pieces back together. It was known that high-pressure cavities are often formed during the bicrystal fusion process. The results of strain mapping near these defects in the next section confirm that the material surrounding the defects is highly stressed.

4.2. Strain patterns associated with bicrystal boundary defects

As a cubic perovskite crystal (*m3m*), $SrTiO_3$ is optically isotropic with negligible absorption in the visible range. Presence of strain fields will, however, change the refractive index. Thus, a non-zero birefringence, the difference in refractive index (Δn) experienced by the two eigen-polarizations, is a quantitative measure of local anisotropic strain fields. The PM-NSOM technique outlined in Section 2.4 was employed to map strain fields associated with the bicrystal boundaries and the microstructural defects discussed in the previous section.

Fig. 17 depicts the (a) topographic, (b) transmission NSOM and (c) near-field retardance (ϕ) image of two defects in a 24° $SrTiO_3$ bicrystal. The ϕ is related to Δn by $\Delta n = \lambda\phi/2\pi d$, where λ is the wavelength of light and d the distance over which the change in phase is acquired. Though the light travels through the entire thickness of the sample, only features within approximately λ of the surface cause changes in NSOM images over the small scan size of the images. The bulk of the crystal contributes an overall background, and features beyond λ can produce slowly varying changes only. The ϕ image, however, has structures as small as ~100 nm. Therefore, these features must be due to strain fields near the surface. For these features of interest, then, we take $d \sim \lambda$. This results in a maximum Δn of 0.014 for the defects on the 24° $SrTiO_3$ bicrystals and 0.035 for defects on the 36° $SrTiO_3$ bicrystal. The strain ε associated with Δn for a cubic material is given by

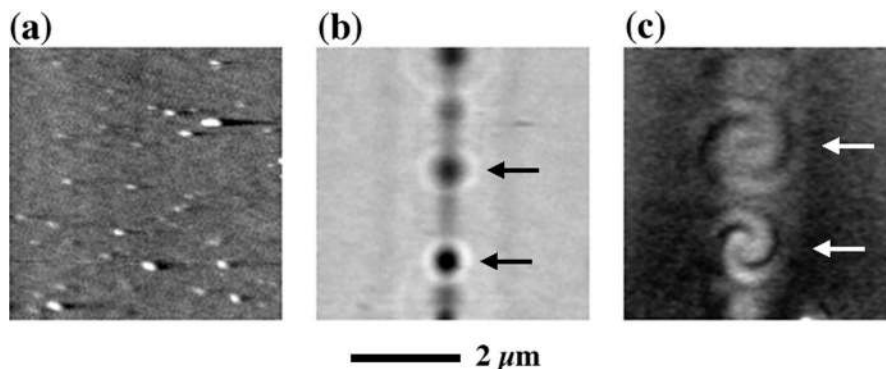

Fig. 17. (a) Topographic, (b) NSOM transmission, and (c) near-field birefringence images of a 24° $SrTiO_3$ bicrystal taken near the fusion boundary. The arrows mark the same positions on the sample. They are slightly displaced between (b) and (c) because the two images were not taken simultaneously. The grayscale in (a) is 30 Å. Features in the topographic image are dust particles. The boundary runs vertically in the center of the images, as can be seen in the transmission NSOM image (b). The lower dark spot in (b) has an optical contrast of 12%, while the upper one has a contrast of 7.2% [172].

$\varepsilon = 2\Delta n/n^3(p_{11}-p_{12})$ [177], where p_{11} and p_{12} are photoelastic constants for $SrTiO_3$ and the index of refraction $n = 2.376$ for $SrTiO_3$ at $\lambda = 670$ nm [178]. This relation is only strictly true for cases when the strain is compressive or tensile and aligned with the [1 0 0] or [0 1 0] crystallographic directions. For compressive or tensile strains aligned with the [1 1 1] or shear strains, $p_{11} - p_{12}$ is replaced by $2p_{44}$ [177]. Other types of strain must be expressed in terms of these components. For $SrTiO_3$ $2p_{44} = 0.144$ and $p_{11} - p_{12} = 0.055$ [179]. Since stress is not applied externally, the direction of the strain is not known in this experiment. Therefore, an average value for the photoelastic constant is used. Using $\varepsilon = 2\Delta n/n^3(p_{ave})$ and taking $p_{ave} \sim 0.1$, the strain associated with the defects can be calculated within a factor of 2. The maximum strain associated with defects found on the 24° $SrTiO_3$ bicrystals is then approximately 0.021, and the maximum strain associated with defects on the 36° $SrTiO_3$ bicrystal is 0.052.

Note that the lateral dimensions of the retardance patterns in Fig. 17(c) are larger than the physical defect sizes appearing in the transmission NSOM image (b). This is expected because strain fields propagate beyond the defects themselves. From Fig. 17(c), it is evident that at the location of the defect, ϕ does not decay monotonically away from boundary, but oscillates. The low ϕ regions between two high ϕ regions are nodal planes (lines) between a compressive and a tensile region. This non-monotonic dependence can only result from multiple sources of strain. In this case, strains from both the void and the fusion boundary contribute. When linecuts perpendicular to the boundary are taken well away from the defects, we find that ϕ does decay monotonically from a non-zero value at the fusion boundary to the background value, further supporting that the oscillations in ϕ near the defects are the result of both voids and boundary. The retardance pattern of a given defect is reproducible when imaged with different tips.

The spiral shape of the strain patterns is unexpected, in that it breaks the reflection symmetry of the boundary. Similar spiral patterns were found to accompany many, though not all, defects on the 24° $SrTiO_3$ bicrystals. Inclusions with different thermal contraction constants or different lattice constants in a bulk cubic crystal result in two- or four-fold symmetric patterns [180] and not the symmetry-breaking strain patterns observed here. However, the defects we study in this paper are not solid inhomogeneities, but are voids that were formed at high temperatures during the fusion process. The surface tension of the surrounding $SrTiO_3$ surfaces plays a role in determining residual strain when the samples are cooled down. The presence of a bicrystal boundary makes the problem even more complicated because the elastic constants change abruptly at the boundary due to a change in the crystallographic direction. Furthermore, using NSOM we are probing near-surface defects. The surface may allow the strain from the defect to relax. In addition, the physical and chemical properties of the surface region might be different from the bulk. Non-cubic strontium and titanium rich phases near the surface have been observed to form at the elevated temperatures [181]. We also found that defects with clear spiral patterns in the same batch of 24° samples all show the same handedness. This implies a connection to some macroscopic phenomenon, such as a twisting motion between the two halves of the bicrystal after the fusion process has initiated. Despite the spiral shape, the observed retardance patterns are not due to screw dislocations. Modeling the sample as a cubic crystal with no boundary, our calculations show that the spiral shape cannot be explained by the birefringence associated with the strain field from a dislocation [182] in the bulk. Furthermore, TEM results do not show screw dislocations in $SrTiO_3$ bicrystals of such large tilt angles.

4.3. YBCO grain boundary Josephson junctions (GBJJs)

After detailed characterization of a 24° $SrTiO_3$ bicrystal, a ~40 nm thick YBCO film was deposited by 90° off-axis sputtering [183]. The film was thin enough to have appreciable optical

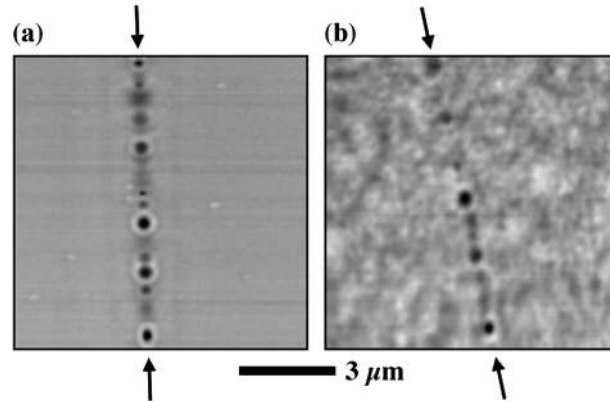

Fig. 18. Transmission NSOM images of (a) a 24° $SrTiO_3$ bicrystal substrate, and (b) the same region after 40 nm of YBCO film has been deposited on the substrate. There is an orientational offset between the two images. The grain boundaries are marked by arrows. Circular dark spots are seen in both images [170].

transmission for NSOM studies. The resistive T_c was 88 K with current parallel to the grain boundary and 81 K across the boundary. The transition width was <2 K in both cases. Ultimately, five GBJJs were patterned across the grain boundary.

Fig. 18 shows transmission NSOM images through the same region of the substrate fusion boundary taken (a) prior to deposition of the YBCO film, and (b) after deposition. The YBCO film well away from the boundary has rms roughness of ~40 Å, as measured by SFM. The background light and dark mottling in Fig. 18(b) is due to the small thickness variations in the YBCO film. The dark defects seen at the YBCO grain boundary in Fig. 18(b) have a one-to-one correspondence with the substrate defects of Fig. 18(a). They are either the same bicrystal substrate defects discussed in Section 4.1 or are caused by these substrate defects.

Whether in the substrate or in the YBCO, these defects directly affect the structure of the YBCO grain boundary as shown in Fig. 19. At the grain boundary, topographic images show that the YBCO thickness can be depressed by 50–200 Å. While defects do not appear in the topographic images, they appear as dark spots in NSOM images. Strikingly, evident is the fact that the grain boundary wanders sharply away from the fusion boundary near the defect, even though the underlying fusion boundary is straight. Boundary wandering in YBCO by >0.5 μm was seen. The paths of the

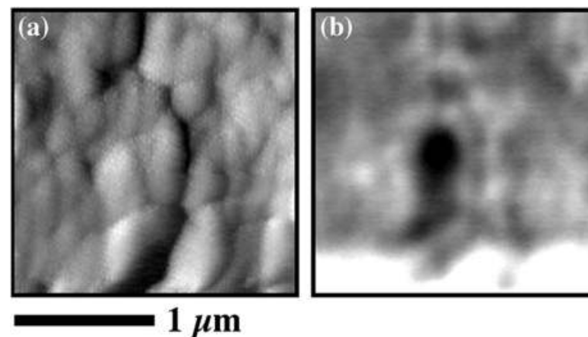

Fig. 19. (a) Topographic and (b) NSOM transmission (2 μm × 2 μm) images taken near a microstructural defect on a 24° $SrTiO_3$ bicrystal with a 40 nm YBCO film. In (a), the YBCO grain boundary is clearly seen to deviate from the fusion boundary around a defect (dark spot in (b)). The grayscale represents 50 Å height change in (a) and 35% contrast in (b) [171].

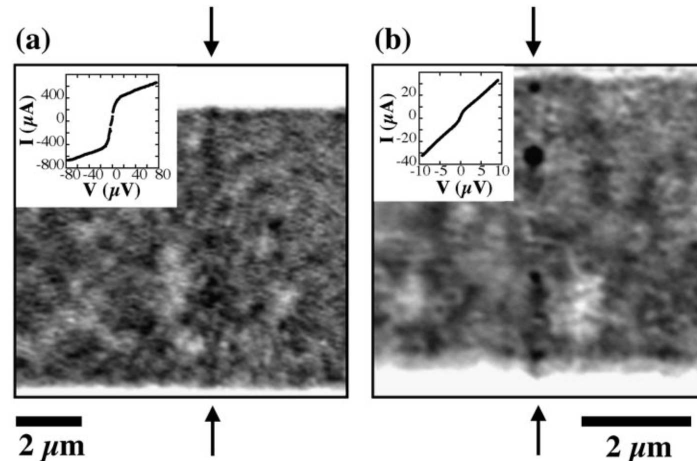

Fig. 20. (a) NSOM image of the ''good'' Josephson junction. Inset: I–V characteristics at 77 K; (b) NSOM image of an adjacent junction. Inset: I–V characteristics at 63 K. The arrows indicate the locations of the grain boundaries [170].

boundary often follow the low strain regions (dark areas in Fig. 17(c)) around the defect. It is evident that the defect-induced distortion of the $SrTiO_3$ lattice as discussed in Section 4.2 has a strong influence on the growth of a YBCO film. While TEM work observed YBCO grain boundary wandering previously, NSOM studies [170,171] are the first to link boundary wandering to substrate defects.

Because the defects are not evenly distributed along the length of the grain boundary, the microstructure of the five Josephson junctions patterned from this film differed. NSOM and SFM showed that by good fortune, one 10 μm wide junction had no detectable defects, little topographic change, and no observable wandering of the grain boundary. An NSOM image of this junction is shown in Fig. 20(a). From a structural standpoint, we term this a ''good'' junction. An NSOM image of an adjacent junction is shown in Fig. 20(b). Defects are clearly evident.

After the NSOM and SFM characterization, the junctions were immersed in liquid nitrogen to measure their electrical properties. The junction in Fig. 20(b) showed ohmic current–voltage (I–V) characteristics at 77 K, but with low resistances of $\sim$1 Ω. A supercurrent became evident only after reducing the temperature to 63 K. As shown in the inset of Fig. 20(b), a distinct though thermally rounded Josephson I–V then appears. Given the degree of thermal broadening, we estimate the I_c in this junction to be 2–3 μA at 63 K. By contrast, the good junction showed a strong Josephson I–V at 77 K (inset of Fig. 20(a)). For this junciton $I_c \approx 380$ μA, two orders of magnitude larger, and $R \approx 0.25$ Ω at 77 K, giving a reasonable I_cR product of $\sim$100 μV. From magnetic field induced I_c modulation patterns, it was deduced that the supercurrent density distribution is more or less across the entire junction, but peaks at the center [170].

In summary, this series of experiments demonstrated clear qualitative correlations among the local structure of the substrate, the microstructure of the YBCO grain boundary, and the electrical quality of the GBJJs. One conclusion is that to a large extent, GBJJ performance and uniformity can be traced directly back to the substrate. Structural quality of the bicrystal fusion boundary at the submicron scale is one, perhaps principal, factor in determining GBJJ characteristics. It is evident that non-uniformly distributed grain boundary defects prevent such GBJJs from having predictable characteristics. Defect-induced strain has a crucial effect on YBCO film growth and HTSC device performance. Since these defects are process related and hence extrinsic, improvements in the bicrystal substrate quality, and thus HTSC GBJJ devices, can be expected.

5. Semiconductors

5.1. III-nitride systems

III-nitride materials (GaN, AlN, and InN) have potential applications in optoelectronics, high-speed and high-temperature electronics. In the past few years, a great deal of the scientific interest and technological advances in this field have been stimulated by the successful realization of UV and blue light emitting diodes and laser diodes based on InGaN/GaN materials [184]. Because there are no well lattice-matched substrates, GaN films grown on sapphire or SiC wafers contain high densities of dislocations, $\sim 10^{10}\ \mathrm{cm}^{-2}$. In addition, they contain high levels of impurities and point defects so that unintentionally doped films are usually n-type with background carrier densities of $\geq 10^{17}\ \mathrm{cm}^{-3}$. One common defect-related feature in GaN films is the broad sub-bandgap luminescence around 550 nm, hence called yellow luminescence (YL). The origin of this deep level transition has been associated with dislocations [185], point defects, and/or impurity complexes [186]. Moreover, In compositions in InGaN films are believed to vary so that light emission might come from localized areas [187]. To further investigate these issues, spatially resolved techniques with nanometer resolution are needed.

NSOM has been used to better understand the origin of YL and the role of dislocations and defects on PL. Here the capability to simultaneously acquire topographic images with optical images and/or spectra proves to be very powerful. Liu et al. found that the high YL emission correlates with step edges in GaN films while the band-edge luminescence does not. They proposed that the deep levels associated with YL arise from impurities, e.g. Si and/or O [188]. Recently, this has been confirmed by a CL and NSOM PL study of selective area epitaxially grown GaN hexagonal pyramids. YL was found to come predominantly from the apex regions of the pyramids, while band-edge emission comes from the entire pyramids. Since the apex regions are free of dislocations as shown by TEM, the authors concluded that YL cannot be the intrinsic property of dislocation defect states, rather it is due to impurities concentrated at the growth front [189]. Crowell et al. also found that sub-bandgap green light emission in InGaN QW films is localized in hexagonal pits while band-edge luminescence is strongest around the edges of these defects [190].

To probe spatial inhomogeneity in carrier transport, Vertikov et al. used an interference technique to excite carriers in a grating pattern and an NSOM tip to collect the resulting spatially varying PL signals [191]. From the PL profiles, they determined the effective ambipolar diffusion length and found that it is spatially varying. In addition to spatial variations, they found that PL profiles in InGaN multiple QWs are very complicated and depend on the emission wavelength. Combining this type of measurements with spatial-averaging time-resolved PL decay measurements, which probe carrier recombination dynamics (e.g. lifetime), the authors measured the diffusion constant. They show evidence that low energy carriers, which result in longer-wavelength emission, are localized in the band-tail states and that these states are filled first at low excitation levels. These results have implications in the operation of LEDs and laser diodes [192].

It is natural to use NSOM to probe the model of In clustering and hence localized emission in InGaN films and QWs. While the band-edge emission definitely shows intensity variations, of order 10–50%, there are no significant spectral changes at different sample positions [190,193,194]. Typical band-edge luminescence peaks from InGaN films or QWs are quite broad (FWHM of order 200 meV). If the light emission originates from localized regions, this broadening is inhomogeneous. By restricting the excitation and/or detection volume, one would expect the broad PL peak to break up into many sharp peaks. This is indeed the case for GaAs/AlGaAs QWs [134,195]. However, this is not seen in InGaN/GaN systems. Moreover, if In composition varies, one would expect to see a

spectral shift in the band-edge peak yet no discernible spectral shifts have been observed with current NSOM resolution ($\sim$100 nm). Hence, if there are In clusters and/or localized emission, the length scale is probably 10 nm and the density would be quite high so that at the 100 nm level the spectra are the same as the spatially averaged result. The In clustering picture still awaits experimental confirmation. Also, the physical origin of the band-edge PL intensity fluctuations in III-nitride materials, as seen in NSOM images, is currently not understood.

5.2. Spatial variations in ordered–disordered (GaIn)P films

(GaIn)P is used in a wide variety of optoelectronic applications. It was found that, under certain growth conditions, group III atoms in (GaIn)P spontaneously order with Ga and In occupying alternate {1 1 1} planes. The ordering reduces the bandgap energy and produces a distinct hillock surface morphology. Spatially averaged PL measurements also show a low energy peak that displays non-exponential temporal dynamics and anomalous intensity and temperature dependence. Using an NSOM to collect PL from a partially ordered (GaIn)P film, Gregor et al. found an anticorrelated spatial dependence among regions emitting bandgap luminescence and those emitting low energy. They also showed variations in linewidth, peak intensity, and peak energies of the low energy luminescence at different positions [82]. By imaging PL at different wavelengths, Leong et al. were able to spatially map ordered and disordered regions on the cleaved side of a partially ordered (GaIn)P sample. By correlating PL intensity and capacitance changes, the authors concluded that the surface Fermi level at the ordered regions was pinned while that at the disordered regions was not pinned [83]. Using vicinal GaAs substrates, completely ordered (GaIn)P films can be grown consisting of a single variant or two variants. Again imaging on the cleaved side, Leong et al. found that PL and capacitance changes for the single-variant sample were uniform while PL and capacitance changes displayed vertical domain structure in the two-variant sample. The size of these domains was small near the substrate, and increased as the film grew thicker. These domains were alternately n-type and p-type according to capacitance measurements. NSOM PL imaging showed that PL came from the n-type regions only. Fig. 21 shows cross-sectional images of a two-variant sample. It is evident that strong PL only comes from larger n-type domains. Furthermore, the PL peak energy shifted to longer wavelengths and the intensity grew stronger as the film grew thicker, indicating that both PL efficiency and ordering improved as the film grew [196]. This work clearly demonstrates the power and application of NSOM to study submicron domain structures in inhomogeneous materials and nanostructures.

5.3. Polycrystalline II–VI thin films

Polycrystalline II–VI thin films are potential candidates for inexpensive solar cells. Two commonly used materials as light absorbing layers are $CuInSe_2$ and CdTe. Both are p-type materials. The n-type CdS is used in both cases to form heterojunctions. Since these materials are granular, questions about the grain boundaries (GBs) physical and chemical nature and their roles in carrier recombination naturally arise. However, since the grain sizes in these thin films are typically 0.5 μm or less, high-resolution techniques are required. McDaniel et al. performed near-field photovoltage measurements (Section 3.2) on both the planar surface and edge of $CdS/Cu(InGa)Se_2$ devices. They found that efficiency varied from grain to grain and was depressed at GBs [154]. They also found the junction location to be at the $CdS/Cu(InGa)Se_2$ heterojunction interface, rather than inside the $Cu(InGa)Se_2$ layer (i.e. homojunction) as previous EBIC measurements suggested [197]. The discrepancy probably arises from the high injection level used in EBIC. Recently, Herndon et al.

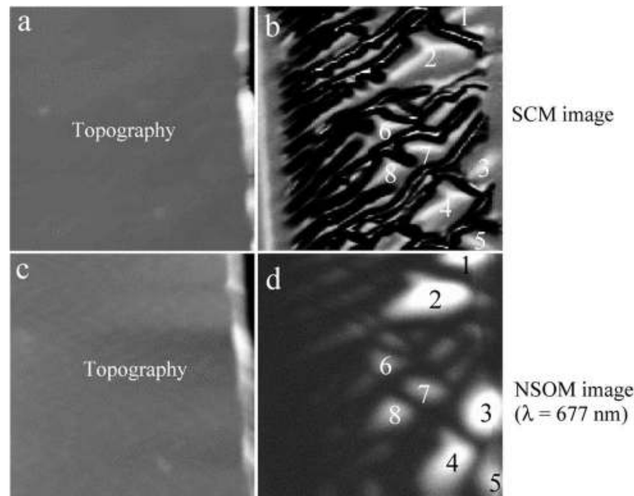

Fig. 21. (a) and (b) Cross-sectional topographic image and simultaneously obtained scanning capacitance image of a two-variant $GaInP_2$ sample. Bright regions in (b) are n-type domains; (c) and (d) represent topographic image and simultaneously obtained PL intensity map ($\lambda = 677$ nm, 3 nm bandwidth) of the same sample. A definite correlation between non-zero PL regions and n-type domains is evident. The image area is 6.5 μm × 8 μm for all images. All images were taken in the same area [196].

studied S diffusion from CdS to CdTe layer by using NSOM to perform local NPC measurements at different excitation wavelengths [92]. The bandgap of Cd(TeS) is lower than that of CdTe for S concentrations less than 25%. NPC images taken with above CdTe bandgap excitation showed that the signal was concentrated near the heterojunction and was uniform along the junction interface. However, when the same image was taken with slightly below-bandgap excitation (corresponding to 6% S in Cd(TeS)), the signal came from most of the CdTe layer and was highly non-uniform. The signal was higher near some GBs. For excitation significantly below bandgap, the NPC signal was very weak and came only from near the CdS/CdTe interface; however, it was highly non-uniform. These observations are consistent with grain-boundary assisted *S* diffusion. Small amounts of *S* are found near GBs deep into the CdTe layer, but high concentrations of *S* are found only near the interface. These two examples show that NSOM is useful in studying granular materials. However, both the NSOM and shear-force resolution is often not high enough for many polycrystalline materials.

5.4. Quantum dots (QDs) grown by strain heteroepitaxy

Quantum nanostructures produced by strain heteroepitaxy have gained significant interest in the past few years. The ability to manipulate electron motions and band structures opens up a wide variety of scientific questions as well as technological applications. In this section, I will focus on QDs resulting from Stranski–Krastanow growth of lattice mismatched materials. Due to the small size (<30 nm laterally) and the high density ($\sim 10^{10}$ cm^{-2}), far-field optical studies measure ensemble averaged properties only, which are dominated by inhomogeneity in the sample. For example, the linewidth of PL peak from QDs is usually many meVs, reflecting the slightly different local environment each dot experiences. This is because there are usually 100–1000 dots under the probe region. Using an NSOM tip, the number of dots probed is of order 10. However, due to the small signal involved, NSOM experiments have so far been done with larger apertures, 150–250 nm. Another challenge of these experiments is that they have to be done at liquid He temperatures.

In spite of formidable technical challenges, much progress has been made recently that demonstrates the value of NSOM studies on QDs. As we discussed in Section 2.3, NSOMs operating in illumination mode and collection mode produce different results because of carrier diffusion. The best results obtained to date on QDs have been done with illumination and collection both through the NSOM apertures [87]. In this operating mode, the linewidth of PL peaks is resolution limited, about 50 μeV [198], which is two orders of magnitude narrower than far-field results. In a InGaAs/AlGaAs system, Chavez-Pirson et al. demonstrated that an image of a single QD can be made with a narrow spectral width around its PL peak. While under the NSOM aperture, there are five sharp PL peaks, the authors showed that the peaks come from five different QDs by analyzing their polarization characteristics. After isolating a single QD, they then varied the pump light intensity dependence to study nonlinear effects. As the pump intensity increased, a second PL peak at 3 meV lower energy became stronger. The intensity of the higher energy PL peak depended on pump intensity linearly while that of the lower energy PL peak depended on pump intensity squared. They attributed the lower energy peak to biexcitonic emission [87]. This information cannot be obtained with far-field measurements because the PL peak is much wider than 3 meV. Toda et al. applied a magnetic field to a InAs/GaAs QD sample and measured Zeeman splitting in individual QDs. From the splitting, they estimated the spatial extent of the carrier wavefunction, which is approximately the same as the size as the QD. They also showed that the Laudau g-factor is different depending on whether the cap layer is GaAs or AlGaAs [197]. In a separate work, they showed that spin relaxation in the excited states can be measured with spin polarized PL experiments [199]. Recently, by performing near-field PLE experiments, Toda et al. found that the carriers relax first within the continuum states and then make transitions to the excitonic ground states by resonant emission of localized phonons [90].

While ground state exciton diffusion causes poor resolution and broad PL spectra under NSOM illumination, it has been shown that the resolution is significantly improved if excited state PL emission images are taken when the ground states are filled [200]. However, one has to be careful with the perturbation the NSOM tip can cause in the QD systems. It has been shown that the force from the tip can stress [85] or modify [201] the sample, resulting in PL spectra changes. Currently, all but one [202] NSOM QD experiment were done on III–V systems.

6. Photonic materials and devices

6.1. Semiconductor laser diodes

In the dawning photonic age, semiconductor laser diodes play an indispensable role in many technological applications, from telecommunications to consumer electronics. It is perhaps obvious that NSOM should be useful for characterization of semiconductor laser diodes because of their small sizes. The active regions of most edge-emitting lasers have a cross section of order 100 nm × 1 μm. In addition, the current blocking layers whose purpose is to channel the carriers to concentrate at the active region have structures on the order of 1 μm. Thus, it requires submicron resolution to map mode profiles and to measure carrier distribution in these devices. Vertical cavity surface emitting laser diodes (VCSELs) are usually larger, with an active region of order 10 μm in diameter. However, the distributed Bragg reflector mirror stacks have periods of order 100 nm and high resolution is needed to resolve the origin of luminescence in these structures. Over the past decade, NSOM has been used to directly map lasing mode profiles above and below threshold in various types of edge emitting laser diodes [88,203–206] and VCSELs [207–209], to quantitatively

measure beam divergence in free space [210], and to characterize spontaneous emission on the cleaved side of VCSELS [211,212]. The two main contributions of NSOM to semiconductor laser diode characterization are high resolution mapping of emission mode profiles and spatially resolved spectral studies to separate different lasing modes and contributions from different origins. In addition, NPC (Section 3.2) microscopy and spectroscopy [151,213] have also been applied to characterize p–n junction quality in laser diodes, which has a direct impact on threshold current and device quantum efficiency.

The first NSOM characterization of semiconductor laser diodes was done in 1991 by Issacson, Cline, and Barshatzky [202]. They used a tapered pipette to collect light from an AlGaAs graded-index separate confinement heterostructure (GRINSCH) laser. While the far field pattern hinted at some asymmetry in the modal profile, the image taken with the tip on the laser facet clearly revealed two bright spots at the two ends of the active region. It should be pointed out here that there is a subtle difference between the usual ‘‘near-field’’ mode field patterns for lasers and the ‘‘near field’’ used in this article. The usual ‘‘near-field’’ mode profiles are taken by placing a lens or objective close to the laser facet, i.e. in the Fresnel regime [214]. In this case, while the mode has not diffracted, the light collected consists of propagating modes only. On the other hand, by placing an NSOM tip at the laser facet, both evanescent and propagating modes are collected. Fig. 21 (taken from [88]) clearly demonstrates the new information that is revealed by NSOM imaging. Fig. 22(a) is taken with an NSOM tip but at 5 μm from the laser surface. This mode profile appears to be perfectly Gaussian. However, the near-field image (Fig. 22(b)) reveals that the emission from the active region is double-lobed and there is InP electroluminescence (not at the lasing wavelength) from a small, probably diffraction limited, spot in the n-InP region [88]. Emission outside of the active region causes undesirable laser characteristics such as lower efficiency, higher threshold, and/or heating. However, since this unwanted emission is spontaneous and not amplified, it is overwhelmed by the lasing emission in the far field and is difficult to characterize with far-field techniques. Lienau et al. showed that the lowest TE and TM modes of a given laser not only have different emission wavelength, they also have different mode dimensions and center positions. The shift of the center position was surprising and was attributed to strain in the structure [205].

In addition to mapping mode profiles, NSOM is very useful when spectral studies of different laser regions are required. Since all semiconductor laser diodes are grown by thin-film epitaxial techniques, the thickness of layers having different compositions, different doping, and/or different

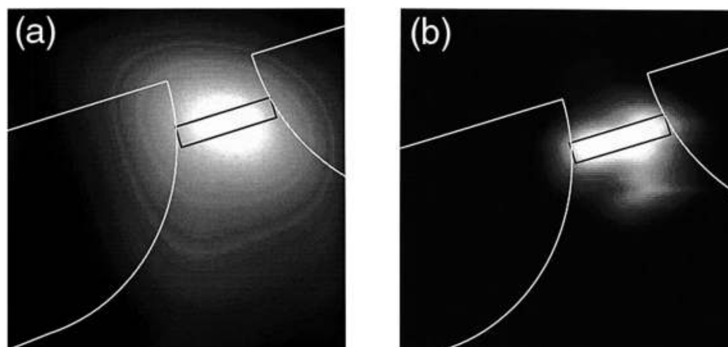

Fig. 22. Far-field vs. near-field image of an InGaAsP multi-quantum well laser electrically driven slightly above threshold: (a) the emission collected by the NSOM tip at a distance of 5 μm from the laser facet surface; (b) the same image acquired with a tip–sample separation of 15 nm. The orientation of the laser structure is shown on each image and the p-InP region is on top [88].

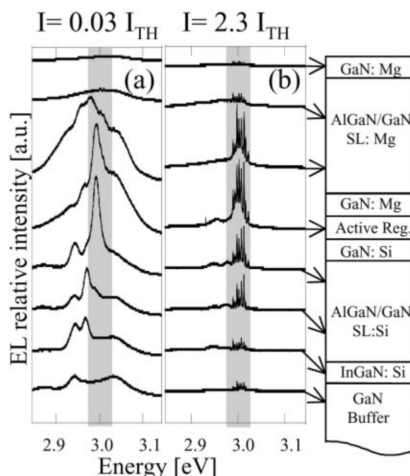

Fig. 23. Representative electroluminescence spectra collected along the cross section (far right) of a three QW InGaN laser structure with a near-field probe: (a) below, and (b) above the lasing threshold. Arrows indicate approximately where spectra were collected (250 nm apart) [206].

function, is typically in the order of tens to hundreds of nanometers. Thus, far field collection typically generates a broad spectrum, but the origin of emission at different wavelengths cannot be isolated. Fig. 23 shows spectra taken at different positions of an InGaN QW laser diode that is electrically pumped below and above threshold [206]. Below threshold, the spontaneous emission spectra are clearly different depending on composition and doping. Above threshold, most emission is centered around 2.97 eV and the peaks are much sharper. However, a significant amount of electroluminescence is not guided within the active region and extends well into the GaN buffer [206]. In an experiment combining the spatial and spectral power of NSOM, the LP_{01} and LP_{11} modes of VCSELs were mapped by forming NSOM images with light collected at different emission wavelengths [208].

There are a few points one should be aware of when interpreting NSOM images of laser diodes. First, emission from guided modes dominates over surface emission in the detected intensity. In the case of studying the cross section of VCSELs, the collected light is mostly from spontaneous emission and not stimulated emission. Hence, the lasing characteristics cannot be studied in this way [212]. Furthermore, carrier diffusion degrades the resolution and surface recombination degrades the total signal in NPC measurements of p–n junctions in lasers. Finally, unless the laser structures are known a priori, it is difficult to interpret the NSOM images.

6.2. Waveguides and fibers

Waveguides and, in particular fibers, form another important component of photonic devices. Knowledge of their index structures, guided mode profiles, and unwanted optical loss is needed to predict and improve the performance of complex optical systems. Even though some waveguides, such as straight channel waveguides and step-index fibers, are simple, their physical properties are difficult to obtain directly due to their small sizes. Characterization of these structures often relies on simulation and measurement of bulk materials. For example, fiber index profiles are done on larger preforms and assumed that a proportional scaling occurs during the drawing process. Often, fabrication processes such as fiber drawing and deposition of cladding materials by modified chemical vapor deposition or frame hydrolysis can alter index profiles. In addition, guided modes

inside waveguides are in general inaccessible to characterization. Far-field transmission and reflection measurements can only indirectly tell us the optical intensity distribution inside the devices. Thus, direct measurement of the actual waveguide modes is essential. NSOM has made many invaluable contributions to this end, which I will summarize in this section. With increased knowledge and experience on fibers and waveguides, NSOM will bring new understanding to more complex optical devices, e.g. microcavities, gratings, and wavelength division multiplexing devices.

The most important measure for an optical fiber is the mode-field radius (MFR). Other fiber properties, such as splicing and bending losses, can be expressed by MFR. Standard far-field techniques can measure MFR accurately for circularly symmetric waveguides, but it is more difficult when the field distribution is not symmetric, e.g. in polarization-maintaining fibers and in rectangular waveguides with different upper and lower claddings. NSOM has been extensively used to map the mode profiles at the exit face of a single mode fiber [215,216], an elliptical core fiber [217], and a rectangular channel waveguide [218]. The measured profiles in general compared favorably to calculations based on models of index profiles. Taking this a step further, Dhar et al. obtained index profiles near the waveguide by using the measured intensity variations as input to the scalar Maxwell equation [218]. They showed that refractive index change is not sharp at the core and cladding boundaries, indicating that phosphorus diffusion has taken place during the waveguide fabrication.

A more important and interesting application of NSOM is to use the tip to pick up the evanescent tail of guided waves, hence providing a tool to sample the optical intensity distribution inside of the waveguide structures directly. Choo et al. was the first to demonstrate this powerful technique by mapping the intensity above a directional coupler consisting of two ridge channel waveguides [219]. Fig. 24 shows a direct map of optical intensity distribution inside the directional coupler. In addition, by fitting the intensity profile above the waveguide and its decay into the cladding, effective index of the guided modes can be determined [220]. Recently, a modulation method was proposed by Tsai et al. to directly measure the spatial variation of the decay constant of the guided mode [221].

Since 1994, many new results have come out of NSOM measurements. Bourzeix et al. reported the first observation of the Tien effect [222], which is a balance between convergence due to index

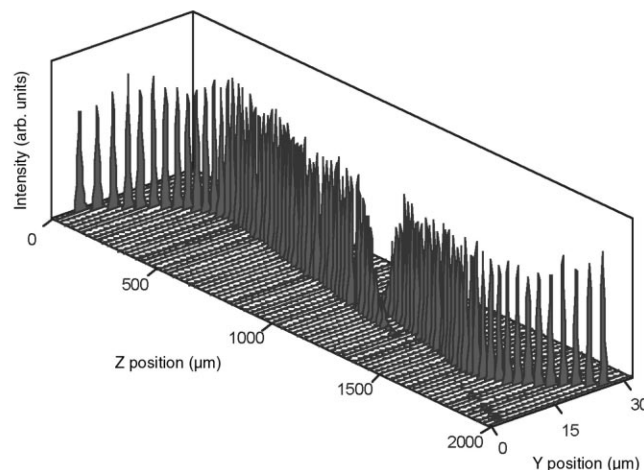

Fig. 24. A three-dimensional (3D) representation of the measured near-field intensity above the directional coupler. Initially only one channel waveguide is excited. At the transition region (where the two waveguides are close), both waveguides carry light. Finally, almost all the optical power is carried by the second waveguide [219].

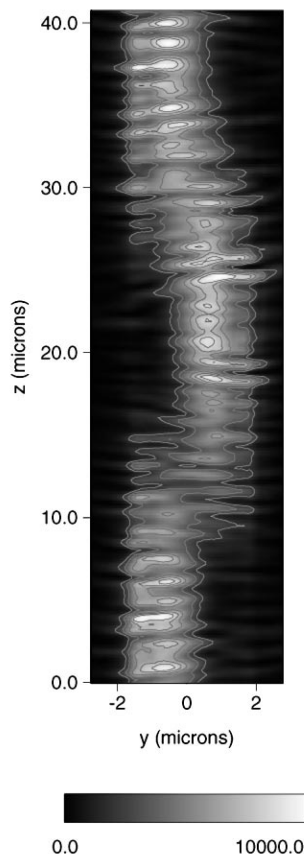

Fig. 25. NSOM image obtained at the surface of the waveguide when TE modes are excited. The standing waves and the beating between TE_0 and TE_1 modes are clearly visible. From these two periods, the effective index experienced by each mode can be determined [225].

gradient in the waveguide and divergence due to diffraction [223]. The optical intensity in the waveguide displays an interference pattern with the contour of high intensity perpendicular to the propagation direction. Realizing this fact, they showed that the effect can be used to map the propagation of guided waves in a complex star couple structure [223].

In addition, standing waves caused by the two faces of straight channel waveguides have been observed using NSOM [220]. From the measured period of the standing waves and the wavelength of the light, the local effective refractive index can be determined unambiguously. Using this result and the transverse mode shape, Vander Rhodes et al. showed that all components of the wave vectors can be obtained [224]. Fig. 25 shows an NSOM image taken at the surface of a buried glass waveguide when TE modes (59% TE_0 and 41% TE_1) are excited. From the period of the standing wave and that of the beating between the two modes, the effective refractive index experienced by each mode was determined. Standing waves were also observed in ring resonators, though it was not expected here because these are traveling wave devices [225]. Recently, for the first time, the whisper gallery modes (WGMs) of a cylindrical optical microcavity have been imaged [226]. As expected, when the cavity is at resonance, the mode field is confined to the cavity edge. However, the authors also reported non-zero intensity at different radial distances, as well as surprising interference patterns. While the excitation light was TE polarized, somehow both TE and TM modes were excited and interfered with each other inside the cavity and generated beating patterns with a period of $\sim$8 μm.

Moreover, the high spatial frequency (190 nm) beating can be explained by the interference of two counter-propagating (clockwise and counter-clockwise) waves. WGMs have not been directly imaged before because of the high Q of these cavities. This work demonstrated a unique capability of NSOM in the characterization of highly confined modes that was not afforded by far-field optical techniques.

Optical losses due to unintentional defects in waveguides are as important as those in laser diodes. At the defect, the guided waves are perturbed and converted to radiation waves that are scattered by the defect. Bourzeix et al. directly observed such a small scattering center, which caused a 0.05 dB power loss and corresponded to a small crack of only 10 nm deep in the shear-force image [223]. Scatterers inside the waveguide also cause interference in addition to exciting lossy leaky modes of the waveguide [227]. Vander Rhodes et al. showed that a spectroscopy technique can be used to analyze internal dielectric interfaces and defects [224].

One concern with NSOM studies of waveguides is whether and how much the presence of the NSOM tip perturbs the guided mode(s). This question has not been addressed quantitatively until recently. When operating in the collection mode, for the NSOM to detect a signal, some amount of the evanescent component of the guided light must be converted to propagating modes by the NSOM tip and coupled to the guided mode of the NSOM fiber. Therefore, the NSOM tip acts as a defect (scatterer) at the surface of the waveguide. In fact, one way to determine whether the guided light or the scattered light is being imaged is to perform an "approach curve," where the NSOM detected intensity is plotted as a function of tip–sample separation. For guided light, as the tip approaches the sample, the signal should increase exponentially with decay constant determined by the wavelength and the effective index. In addition, the metal coating of the NSOM tip poses additional boundary conditions that might modify the mode structures. Previously, the experimental evidence indicated, though indirectly, that the perturbation is small, e.g. the lasing threshold or the resonance wavelength of cavity is not altered. Vander Rhodes et al. performed the first experiment to quantify the perturbation caused by the NSOM measurement. They monitored the transmitted power of the channel waveguide simultaneously as the NSOM tip scanned across it. They found that when the tip is centered on the waveguide, where the optical intensity detected by the NSOM is maximum, the transmitted power decreases by 1% [225]. However, the effect on the guided mode profile is currently unknown. Numerical calculations of NSOM imaging of a photonic crystal also show that the presence of NSOM has little effect on the photonic crystal band structure [228]. Nevertheless, it is prudent to include the NSOM tip in numerical simulations of NSOM experiments.

All the experiments cited above monitor the intensity variations in the near-field. Recently, a direct measurement of the optical phase was demonstrated by incorporating an NSOM into one arm of a Mach-Zehnder interferometer [229]. With this set up, both the phase and the amplitude of the electromagnetic field of the guided wave can be obtained. Phase singularities of charge ± 1 have been imaged in a waveguide [230], see Fig. 26. They occur where the modal field amplitude vanishes, due to the interference of various modes in the waveguide.

6.3. Photonic bandstructure materials

In the past decade, photonic bandstructure materials (or photonic crystals) have generated a great deal of interest, in part due to technological advances that make it possible to fabricate these structures for operation in the visible and near-infrared spectral range. Photonic crystals are structures with periodic dielectric constant (refractive index) variations. Opal is a natural example of such materials. The dispersion of photons in a photonic crystal reflects the underlying crystal structure, i.e. displaying band structure effects, resembling the dispersion of electrons in an atomic

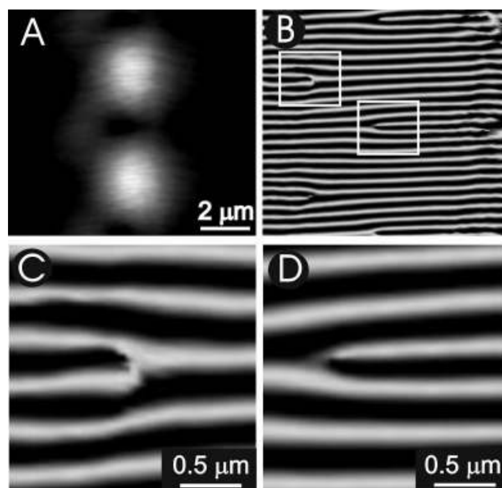

Fig. 26. Interference measurement of a Si_3N_4 channel waveguide for a scan range of 9 μm × 10 μm. Linearly polarized light has been coupled in a controlled way in the channel waveguide to excite the TE and TM modes simultaneously. (A) The measured amplitude of the optical field inside the waveguide. A clear beating pattern is observed. (B) The measured phase evolution of the optical field. The cosine of the phase is shown. Several phase singularities are seen. The zoom in of the left and right box is shown in (C) and (D), respectively. The phase singularity in (C) and (D) is +1 and −1, respectively [230].

crystal [231]. Photonic bandstructure materials provide a new way to manipulate and control light, with applications including waveguiding [232], microcavities [233,234], and lasers [235], to name a few. While theoretical simulations often generate beautiful maps of eigenmode field intensity distributions inside the photonic crystals [231], experimental work has so far concentrated on transmission properties. These reciprocal-space results can provide real-space information only indirectly. Real-space mapping is especially needed in case of defect modes. For example, it would be useful to experimentally verify the calculated defect-mode field distribution, such as what is shown in [236], in a real device. Since the lattice constant of the photonic crystal is of the same order as the wavelength of interest, far-field technique cannot provide sufficient resolution for real-space mapping of optical intensity distributions within a unit cell. Moreover, photonic crystals are often intergrated in a waveguide structure so that the mode of interest is the guided mode. Hence, NSOM characterization provides the unique capability to perform high-resolution real-space imaging of optical intensity distribution inside photonic bandstructure materials.

Despite the obvious utility of NSOM in this area, experimentally mapping optical mode distribution in a photonic crystal has been hampered by technical difficulties [237–239]. The biggest problem comes from not having the ''right'' sample. In the visible, the lattice constant is only two or three times that of NSOM resolution, making resolution an issue. In the infrared, e.g. 1.5 μm, the lack of sensitive detectors makes it difficult to detect the small amounts of light which occur when probing evanescent tails of guided modes. Furthermore, imperfections introduced during the fabrication of photonic crystals cause light to scatter out of the structure, i.e. turning the photonic crystal into a diffractive element. When this happens, NSOM will predominantly pick up free-space propagating modes (scattered light), which overwhelm any evanescent signals [238]. Fig. 27 clearly demonstrates a case of scattered light dominating guided modes. The image is formed by recording NSOM collected intensity along a 1D photonic bandgap structure (x) and varying tip–sample separation (z). The signal collected clearly does not decrease exponentially as for evanescent waves. Moreover, the patterns indicate the sample consists of multiple scatterers. The roughness of the side walls and that of the etched trenches are believed to cause the unwanted scattering in this case [238].

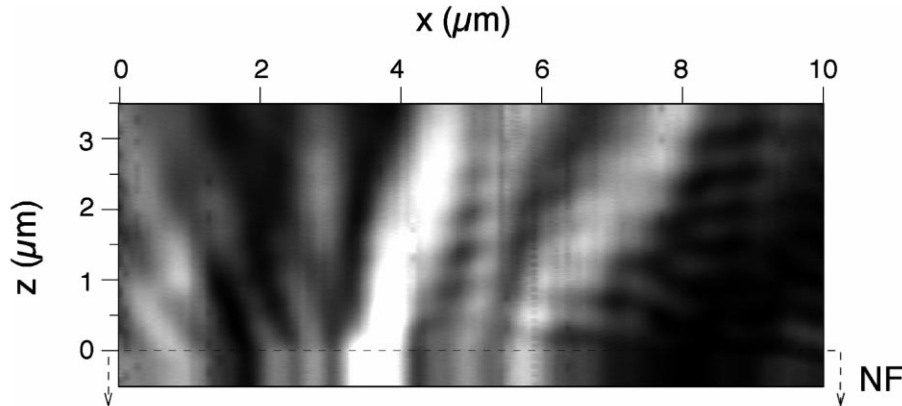

Fig. 27. A grayscale image showing the collected NSOM intensity as a function of both the height above a 1D photonic bandstructure device (z) and along the waveguide (x). The waveguide was excited at 860 nm at the long wavelength band-edge resonance. Note the lack of exponential decay expected in evanescent modes, as well as the overall diffraction pattern typical of multiple in-phase scattering centers ([238] © 1998 IEEE).

Even when the roughness is not an issue, the sudden change of effective refractive index from smooth waveguide region to the photonic crystal region can cause leakage and reflection of guided light. This is especially severe for high index materials and for high index contrast structures. Phillips et al. showed that NSOM collected intensity taken on the surface of the photonic crystal waveguide peaks at the boundary between the smooth region and the photonic crystal region [239]. Both Vander Rhodes et al. [238] and Phillips et al. [239] reported the lack of light penetrating into the photonic crystals, indicating that these samples are highly lossy. Phillips et al. also pointed out that photonic crystals can act as Bragg diffraction gratings and couple light into the substrate, i.e. the light is not guided in the top waveguide. One way to ensure light guided in the waveguide is to make membrane structures [233]. However, on top of the fabrication challenges, it is extremely difficult to couple light efficiently into these small cross-section structures. In addition, to excite eigenmodes in a 2D photonic crystal, a plane wave approximation must be satisfied. Therefore, the beam size is necessarily large, which reduces the fraction of light coupled into the waveguide relative to the unwanted free-space propagating light.

McDaniel et al. performed a transmission NSOM experiment through a nanochannel glass (NCG) sample of 250 μm thickness [237]. The NCG sample consists of a hexagonal array of a high index glass cylinders ($n = 1.68$) embedded in a lower index glass matrix ($n = 1.66$). The channel glass diameter is ~745 nm with center-to-center nearest-neighbor separation of 1.07 ± 0.05 μm. While the index contrast of this structure is too small to exhibit a true photonic bandgap, it has been observed that transmission reduction occurs at frequencies and directions according to its photonic band structure [240]. Fig. 28 shows the transmission images taken on this photonic crystal at two different frequencies and with three different numerical aperture (NA) collection objectives. The transmission through the high index cylinders (channels) is higher in all cases. The contrast decreases with increasing NA. However, it is evident that the transmission at the channels can display structures that are not correlated to index changes and that are dependent on wavelength and collection optic NA. These results were understood by comparison with numerical calculations of a model that includes the entire process of image formation, i.e. the tip field, tip/sample coupling, light propagation through the sample, and light collection [241]. The NSOM light couples to photonic crystal modes of various wave vector (Q), and the light comes out of the sample in directions allowed by the crystal symmetry. When higher NA objective is used, more higher Q modes, i.e. modes

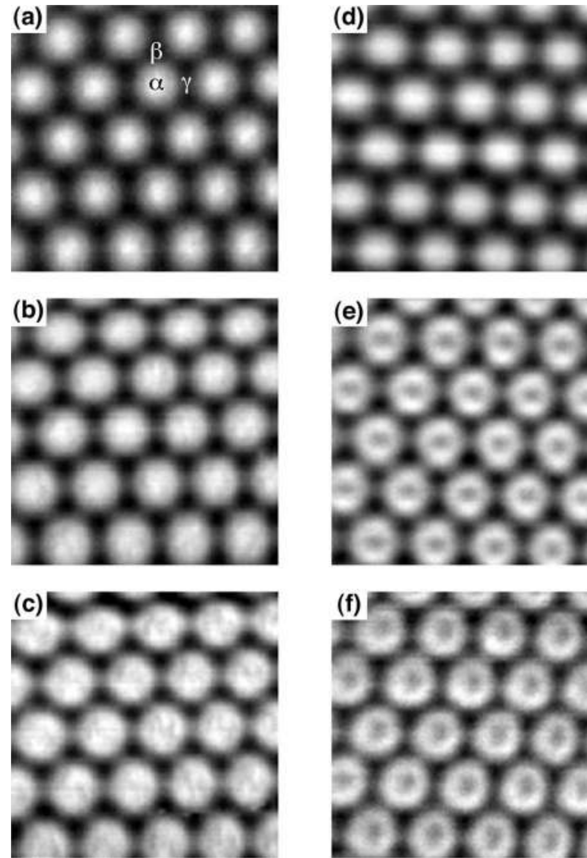

Fig. 28. NSOM images of a NCG array: (a)–(c) were taken with a $\lambda = 670$ nm diode laser, and (d)–(f) were taken with a Argon laser ($\lambda = 488$ nm). The collection objective NA was varied: (a) and (d) $NA = 0.28$, (b) and (d) $NA = 0.55$, and (c) and (f) $NA = 0.70$. The full gray scales represent optical contrast (change in intensity normalized by averaged intensity) of 53, 38, 28, 54, 25, and 15%, respectively, in (a)–(f) [237].

belonging to higher Brillouin zones, are collected. These higher Brillouin zone modes have peak intensity away from channel centers. The wavelength dependence is a result of the cutoff wave vector for a given NA being larger for shorter wavelength. This was the first demonstration that NSOM is useful for characterizing photonic crystals even though the photonic band structure information cannot be readily extracted from the NSOM data.

Based on a computational study, Fan et al. reported that NSOM imaging of a finite photonic crystal not only can map eigenmode intensity distribution, but it can also measure the dispersion relation of the photonic crystal, i.e. frequency versus wave vector (ω vs. k). They showed that in order to probe the photonic crystal modes, the NSOM tip must be strongly coupled to the photonic crystal, and also tested how the presence of the NSOM tip might perturb the mode structures [228]. We recently performed a collection-mode NSOM experiment on a NCG photonic crystal similar to that used in [237], but with a channel diameter of $\sim$135 nm and center-to-center nearest-neighbor distance of 185 nm [242]. This NCG sample has a fundamental pseudo-gap (transmission minimum) at 535 nm. Light of several wavelengths ranging from 488 to 670 nm was launched in the next nearest-neighbor direction, hence probing the photonic crystal in the Γ–X direction (also referred to as G-M direction in some papers) [243]. This is the first experiment that studies the photonic band structure across the fundamental gap or pseudo-gap. Collection NSOM images show high and low

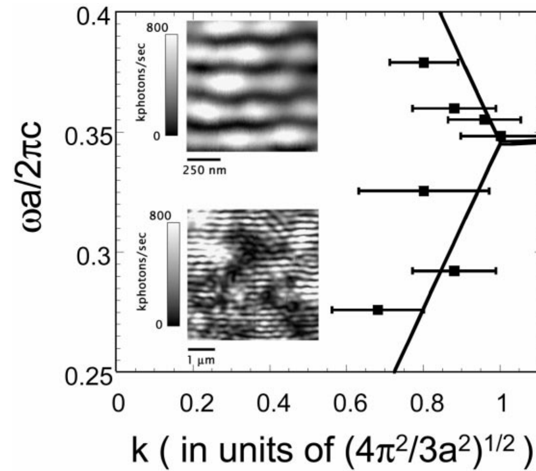

Fig. 29. Dispersion relation (ω vs. k) along the Γ–X direction for NCG array with 135 nm diameter channel glass ($n = 1.68$) in a lower index matrix glass ($n = 1.66$). The lattice constant (a) in the closed packed direction, i.e. center-to-center distance between nearest neighbors, is 185 nm. Γ is at $k = 0$ and X is at $k = 1$. Insets show two representative collection-mode NSOM images taken with 568.2 nm light. The top image is 1 μm × 1 μm and the bottom one is 5 μm × 5 μm. Both short and long period intensity modulations are clearly visible. The solid lines are the result of a numerical calculation using plane wave expansion method [242].

intensity bands perpendicular to the propagating direction (Fig. 29 insets). The spacing of these bands is comparable to the photonic crystal spacing in this direction, 160 nm exhibits a non-montonic wavelength dependence. In addition, larger scale (∼1.5 μm) non-uniformity in the optical intensity was observed, with much stronger contrasts than expected from the small index contrast of the sample. Both observations are explained by the interference inside the photonic crystal between light incoming and reflected from the sample/air exit interface, as described in Ref. 210. From the spacing of the bands and the lattice vector, the wave vector (k) probed by each wavelength was determined. Fig. 29 shows the experimentally determined dispersion relations agree with the calculated results to within the uncertainty of the measurements. Given that the calculation uses only the nominal physical parameters of the sample with no adjustable parameters, the agreement between the experimental and calculated results is significant. Hence, the dispersion relations of the lowest photonic crystal modes can be determined completely from NSOM images. This effect was suggested by Fan et al. [210], but has not been observed experimentally until now.

The above-described experiment further demonstrates the power of NSOM in studying photonic band structure materials. Therefore, despite experimental difficulties, we can expect more successful NSOM studies of photonic crystals and other complicated photonic devices in the near future.

7. Transmission contrast in non-absorbing samples

In this section, I will show examples of difficulty in interpreting NSOM image contrast. In some cases, the contrast is completely opposite to our informed intuitions based on far-field optics. Only by comparison with numerical simulations of *realistic* experimental systems can we begin to understand the physical origins behind these apparently anomalous results.

First, let us examine how NSOM transmission intensity varies across a non-absorbing sample with refractive index changes. Can we obtain relative refractive indices from NSOM transmission images? If possible, we might potentially use NSOM to examine latent patterns in photoresist, and

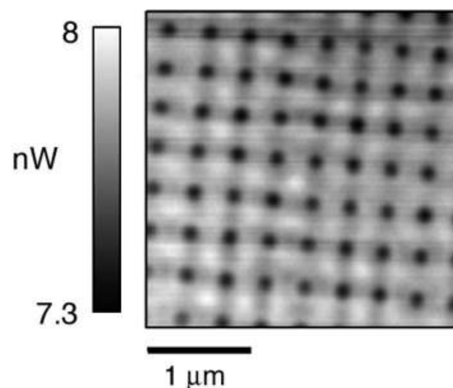

Fig. 30. Transmission NSOM image (3 μm × 3 μm) of an array of air holes (diameter = 80 ± 10 nm) in a 50 nm thick SiN_x membrane. The holes are dark in the imaging, i.e. when the NSOM is directly above the air holes, less light propagates to the far-field [245].

perhaps to fix any problems without going through the developing procedures. McDaniel and Hsu showed that when an NSOM tip is scanned across the boundary of two glasses of slightly different refractive indices (1.66 and 1.68), the contrast is much larger than 1% and *the smaller index material appears dark* [175]. That is, less light is collected in the far field when the NSOM tip is over the smaller index glass. This is certainly against conventional wisdom. Normally, one would expect higher reflection, hence less transmission, when a collimated light beam is incident upon a higher index surface because of the larger index difference between air and the solid. The reflection coefficient difference for two materials with different indices is proportional to their index difference.

An extreme example of this is demonstrated in Fig. 30, in which an NSOM transmission image of air holes in a 50 nm thick SiN_x membrane ($n \sim 2$) is shown. The collection is done with a 100× objective (NA = 0.7). The diameter of holes is ∼80 ± 10 nm, as determined by SEM. It is clear that the air holes are dark, i.e. when the NSOM tip is above the holes, less light propagates to the far-field. This is completely opposite to what one would naively expect. Above the holes, the light propagating out of the NSOM aperture should reach the detector. Above the SiN_x membrane, while some evanescent light will be converted to propagating light in the higher index material, without scattering, these will not be propagating modes on the other side of the membrane and will not reach the detector. Therefore, there should not be significant increases in propagating power for smooth samples. Experimental observation shows that the SiN film away from the holes is smooth. Reflection from the two air/SiN_x interfaces, scattering, and absorption inside SiN_x membrane (though small) all will contribute to reducing, not enhancing, transmission. Recent finite element time domain calculations show that the presence of a dielectric in the near-field zone of a realistic NSOM tip converts evanescent modes to propagating modes, resulting in enhanced transmission [244]. Experimentally, we observed that the degree of enhancement depends on the refractive index and thickness of the dielectric [245].

Another non-intuitive result is that the transmission NSOM images of non-absorbing samples with refractive index variations depend on the NA of the collection objectives. In general, we found that the total collected intensity increases and the image contrast decreases with increased NA. While the former observation is expected, the latter is subtler. The physical reason for the decrease in contrast is that the intensity being re-distributed in different directions due to the scattering by the index variations of the sample. Results of two different index glasses were interpreted in terms of refraction at the boundary [175], which caused light to scattered to larger angles. An astonishing

example of the NA dependence was already shown in Fig. 28 and described in Section 6.3. We want to emphasize that these results were understood only after performing numerical calculations of a model that takes into account *the entire process of image formation*, including the tip field, tip/sample coupling, light propagation through the sample, and light collection [241]. These examples clearly demonstrate the complication and counter-intuitive confusion that can arise when interpreting NSOM image contrast.

8. Summary and future directions

Over the past decade, much progress has been made in both NSOM development and NSOM application to materials characterization. This review can only cover a limited number of examples. While the topographic resolution of NSOM is not as high as that of scanning force microscopy, its usefulness has been clearly demonstrated. In some cases, it offers a unique perspective that simply cannot be obtained by any other characterization technique. Future directions associated with specific examples in the paper have already been pointed out and will not be repeated here. In general, we can expect optical imaging methods with higher resolution. This can be achieved with a revolutionary tip fabrication method or a different approach, such as apertureless NSOM [57]. Of course, high sensitivity detectors will also facilitate advances in obtaining higher resolution. Numerical calculations of realistic systems will become more important because of the need to obtain quantitative understanding of experimental results. Furthermore, near-field imaging will be extended to spectral regimes outside of the visible, e.g. infrared and microwave. As photonics further replaces the role of electronics in network and communications applications, the need to characterize individual components as well as entire optical systems will be increasingly more important. We can expect NSOM to play a big role in this area due to its unprecedented resolution, high sensitivity, and proximity-probe nature.

Acknowledgements

I would like to thank W.S. Fann, B.B. Goldberg, S.K. Buratto, D.D. Awschalom, C.C. Williams, H.E. Jackson, and N.F. van Hulst for providing figures in this review article. I also would like to thank M.H. Gray and A.L. Campillo for their critical readings of this manuscript.

E.B. McDaniel, M.H. Gray, A.L. Campillo, Q. Xu, and A.A. McDaniel were primarily responsible for the near-field optical works done at the University of Virginia. We also were benefited from collaborations with S.C. Gausepohl, C.T. Li, M. Lee, R.A. Rao, C.B. Eom, E.A. Fitzgerald, Y.H. Xie, P.J. Silverman, M. Bulsara, L. Giovane, B.S. Deaver, H.D. Hallen, W.S. Fann, P.K. Wei, S.C. McClain, A.M. Gabor, G.W. Bryant, L.S. Goldner, E.L. Shirley, R.J. Tonucci, C.A. White, A. Rosenberg. Many of the works were supported by National Science Foundation, University of Virginia, Department of Energy, and the Jeffress Memorial Trust. Finally, I would like to acknowledge the support of the Sloan Foundation.

References

[1] G. Binning, H. Rohrer, Ch. Gerber, E. Weibel, Appl. Phys. Lett. 40 (1982) 178.
[2] G. Binning, H. Rohrer, Ch. Gerber, E. Weibel, Phys. Rev. Lett. 49 (1982) 57.
[3] G. Binning, C.F. Quate, Ch. Gerber, Phys. Rev. Lett. 56 (1986) 930.

[4] C.C. Williams, J. Slinkman, W.P. Hough, H.K. Wickramasinghe, Appl. Phys. Lett. 55 (1989) 1662.
[5] Y. Huang, C.C. Williams, J. Vac. Sci. Technol. B 12 (1994) 369.
[6] Y. Martin, D.W. Abraham, H.K. Wickramasinghe, Appl. Phys. Lett. 52 (1988) 1103.
[7] B.D. Terris, J.E. Stern, D. Rugar, H.J. Mamin, Phys. Rev. Lett. 63 (1989) 2669.
[8] Y. Martin, H.K. Wickramasinghe, Appl. Phys. Lett. 50 (1987) 1455.
[9] J.J. Saenz, N. Garcia, P. Grutter, E. Meyer, H. Heinzelmann, R. Wiesendanger, L. Rosenthaler, H.R. Hidber, H.J. Guntherodt, J. Appl. Phys. 62 (1987) 4293.
[10] D.W. Pohl, W. Denk, M. Lanz, Appl. Phys. Lett. 44 (1984) 651.
[11] A. Harootunian, E. Betzig, M. Isaacson, A. Lewis, Appl. Phys. Lett. 49 (1986) 674.
[12] E.H. Synge, Philos. Mag. 6 (1928) 356.
[13] E.A. Ash, G. Nicholls, Nature 237 (1972) 510.
[14] R.C. Reddick, R.J. Warmack, T.L. Ferrell, Phys. Rev. B 39 (1989) 767.
[15] D. Courjon, K. Sarayeddine, M. Spajer, Opt. Commun. 71 (1989) 23.
[16] E. Betzig, J.K. Trautman, T.D. Harris, J.S. Weiner, R.L. Kostelak, Science 251 (1991) 1468.
[17] E. Betzig, P.L. Finn, J.S. Weiner, Appl. Phys. Lett. 60 (1992) 2484.
[18] R. Toledo-Crow, P.C. Yang, Y. Chen, M. Vaez-Iravani, Appl. Phys. Lett. 60 (1992) 2957.
[19] E. Betzig, R. Chichester, Science 262 (1993) 1422.
[20] J.K. Trautman, J.J. Macklin, L.E. Brus, E. Betzig, Nature 369 (1994) 40.
[21] S.K. Buratto, Current Opinion in Solid State Mater. Sci. 1 (1996) 485.
[22] Ch. Lienau, T. Elsaesser, Ultrafast Physical Processes in Semiconductors, Semiconductors, Semimetals, Vol. 67, Academic Press, Boston, 2001, p. 39.
[23] R.C. Dunn, Chem. Rev. 99 (1999) 2891.
[24] S. Kirstein, Current Opinion in Colloid Interface Sci. 4 (1999) 256.
[25] J.D. McNeill, D.B. O'Connor, P.F. Barbara, J. Chem. Phys. 112 (2000) 781.
[26] D.W. Pohl (Ed.), Near Field Optics, Daniel Courjon, NATO ASI Series E: Applied Sciences, in: Proceedings of NATO Advance Research Workshop on NFO, 26–28 October 1992, Kluwer Academic Publishers, Dordrecht, 1993.
[27] M.A. Paesler, P.J. Moyer, Near-Field Optics, Wiley, New York, 1996.
[28] J.W.P. Hsu, Mater. Res. Soc. Bull. 22 (1997) 27.
[29] G.A. Valaskovic, M. Holton, G.H. Morrison, Appl. Opt. 34 (1995) 1215.
[30] E.B. McDaniel, S.C. McClain, J.W.P. Hsu, Appl. Opt. 101 (1998) 84.
[31] C.W. Hollars, R.C. Dunn, Rev. Sci. Instrum. 69 (1998) 1747.
[32] S. Pilevar, K. Edinger, W. Atia, I. Smolyaninov, C. Davis, Appl. Phys. Lett. 72 (1998) 3133.
[33] J.A. Veerman, A.M. Otter, L. Kuipers, N.F. van Hulst, Appl. Phys. Lett. 72 (1998) 3115.
[34] D.I. Kavaldjiev, R. Toledo-Crow, M. Vaez-Iravani, Appl. Phys. Lett. 67 (1995) 2771.
[35] M. Stahelin, M.A. Bopp, G. Tarrach, A.J. Meixner, I. Zschokke-Granacher, Appl. Phys. Lett. 68 (1996) 2603.
[36] R.M. Stockle, N. Schaller, V. Deckert, C. Fokas, R. Zenobi, J. Microscopy 194 (1999) 378.
[37] S. Mononobe, M. Ohtsu, J. Lightwave Technol. 14 (1996) 2231.
[38] P. Hoffmann, B. Dutoit, R.P. Salathe, Ultramicroscopy 61 (1995) 165.
[39] P. Lambelet, A. Sayah, M. Pfeffer, C. Philipona, F. Marquis-Weible, Appl. Opt. 37 (1998) 7289.
[40] R. Stockle, C. Fokas, V. Deckert, R. Zenobi, Appl. Phys. Lett. 75 (1999) 160.
[41] S.J. Bukofsky, R.D. Grober, Appl. Phys. Lett. 71 (1997) 2749.
[42] A.G.T. Ruiter, M.H.P. Moers, N.F. van Hulst, M. de Boer, J. Vac. Sci. Technol. B 14 (1996) 597.
[43] W. Noell, M. Abraham, K. Mayr, A. Ruf, J. Barenz, O. Hollricher, O. Marti, P. Guthner, Appl. Phys. Lett. 70 (1997) 1236.
[44] H. Zhou, A. Midha, G. Mills, L. Donaldson, J.M.R. Weaver, Appl. Phys. Lett. 75 (1999) 1824.
[45] N.F. van Hulst, M.H.P. Moers, O.F.J. Noordman, R.G. Tack, F.B. Segerink, B. Bolger, Appl. Phys. Lett. 62 (1993) 461.
[46] M. Radmacher, P.E. Hillner, P.K. Hansma, Rev. Sci. Instrum. 65 (1994) 2737.
[47] L. Malmqvist, H.M. Hertz, Opt. Commun. 94 (1992) 19.
[48] T. Sugiura, T. Okada, Y. Inouye, O. Nakamura, S. Kawata, Opt. Lett. 22 (1997) 1663.
[49] O. Sqalli, M.P. Bernal, P. Hoffmann, F. Marquis-Weible, Appl. Phys. Lett. 76 (2000) 2134.
[50] M. Specht, J.D. Pedarnig, W.M. Heckl, T.W. Hansch, Phys. Rev. Lett. 68 (1992) 476.
[51] T.J. Silva, S. Schultz, D. Weller, Appl. Phys. Lett. 65 (1994) 658.
[52] M. Ashino, M. Ohtsu, Appl. Phys. Lett. 72 (1998) 1299.
[53] R. Kopelman, W. Tan, Appl. Spec. Rev. 29 (1994) 39.
[54] S.A. Vickery, R.C. Dunn, Biophys. J. 76 (1999) 1812.
[55] A. Partovi, D. Peale, M. Wuttig, C.A. Murray, G. Zydzik, L. Hopkins, K. Baldwin, W.S. Hobson, J. Wynn, J. Lopata, L. Dhar, R. Chichester, J.H.J. Yeh, Appl. Phys. Lett. 75 (1999) 1515.
[56] S. Heisig, O. Rudow, E. Oesterschulze, Appl. Phys. Lett. 77 (2000) 1071.
[57] F. Zenhausern, Y. Martin, H.K. Wichramasinghe, Science 269 (1995) 1083.
[58] E.J. Sanchez, L. Novotny, X.S. Xie, Phys. Rev. Lett. 82 (1999) 4014.

[59] H.F. Hamann, A. Gallagher, D.J. Nesbitt, Appl. Phys. Lett. 73 (1998) 1469.
[60] C. Hueber, J. Levy, Appl. Phys. Lett. 73 (1998) 3229.
[61] C.C. Wei, P.K. Wei, W.S. Fann, Appl. Phys. Lett. 67 (1995) 3835.
[62] M. Garcia-Parajo, E. Cambril, Y. Chen, Appl. Phys. Lett. 65 (1994) 1498.
[63] J.K. Leong, C.C. Williams, Appl. Phys. Lett. 66 (1995) 1432.
[64] J.W.P. Hsu, M. Lee, B.S. Deaver, Rev. Sci. Instrum. 66 (1995) 3177.
[65] K. Karrei, R.D. Grober, Appl. Phys. Lett. 66 (1995) 1842.
[66] W.A. Atia, C.C. Davis, Appl. Phys. Lett. 70 (1997) 405.
[67] H. Edwards, L. Taylor, W. Duncan, A.J. Melmed, J. Appl. Phys. 82 (1997) 980.
[68] M. Lee, E.B. McDaniel, J.W.P. Hsu, Rev. Sci. Instrum. 67 (1996) 1468.
[69] J.W.P. Hsu, A.A. McDaniel, H.D. Hallen, Rev. Sci. Instrum. 68 (1997) 3093.
[70] F.F. Froehlich, T.D. Milster, Appl. Phys. Lett. 65 (1994) 2254.
[71] M.J. Gregor, P.G. Blome, J. Shcofer, R.G. Ulbrich, Appl. Phys. Lett. 68 (1996) 307.
[72] K. Hsu, L.A. Gheber, Rev. Sci. Instrum. 70 (1999) 3609.
[73] M.A.D. Roby, G.C. Wetsel, Appl. Phys. Lett. 69 (1996) 3689.
[74] P.K. Wei, W.S. Fann, J. Appl. Phys. 83 (1998) 3461.
[75] F.F. Froehlich, T.D. Milster, Appl. Phys. Lett. 70 (1997) 1500.
[76] T. Okajima, S. Hirotsu, Appl. Phys. Lett. 71 (1997) 545.
[77] P.K. Wei, W.S. Fann, J. Appl. Phys. 87 (2000) 2561.
[78] B. Hecht, H. Bielefeldt, Y. Inouye, D.W. Pohl, L. Novotny, J. Appl. Phys. 81 (1997) 2492.
[79] K.D. Weston, S.K. Buratto, J. Phys. Chem. B 101 (1997) 5684.
[80] C.E. Jordan, S.J. Stranick, L.J. Richter, R.R. Cavanagh, J. Appl. Phys. 86 (1999) 2785.
[81] R.D. Grober, T.D. Harris, J.K. Trautman, E. Betzig, W. Wegscheider, L.N. Pfeiffer, K.W. West, Appl. Phys. Lett. 64 (1994) 1421.
[82] M.J. Gregor, P.G. Blome, R.G. Ulbrich, P. Grossmann, S. Grosse, J. Feldmann, W. Stolz, E.O. Gobel, D.J. Arent, M. Bode, K.A. Bertness, J.M. Olson, Appl. Phys. Lett. 67 (1995) 3572.
[83] J.K. Leong, J. McMurray, C.C. Williams, G.B. Stringfellow, J. Vac. Sci. Technol. B 14 (1996) 3113.
[84] J. Levy, V. Nikitin, J.M. Kikkawa, A. Cohen, N. Samarth, R. Garcia, D.D. Awschalom, Phys. Rev. Lett. 76 (1996) 1948.
[85] H.D. Robinson, M.G. Muller, B.B. Goldberg, J.L. Merz, Appl. Phys. Lett. 72 (1998) 2081.
[86] T.D. Harris, D. Gershoni, R.D. Grober, L. Pfeiffer, K. West, N. Chand, Appl. Phys. Lett. 68 (1996) 988.
[87] A. Chavez-Pirson, J. Tammyo, H. Kamada, H. Gotoh, H. Ando, Appl. Phys. Lett. 72 (1998) 3494.
[88] S.K. Buratto, J.W.P. Hsu, J.K. Trautman, E. Betzig, R.B. Bylsma, C.C. Bahr, M.J. Cardillo, J. Appl. Phys. 76 (1994) 7720.
[89] S.A. Safvi, J. Liu, T.F. Kuech, J. Appl. Phys. 82 (1997) 5352.
[90] Y. Toda, O. Moriwaki, M. Nishioka, Y. Arakawa, Phys. Rev. Lett. 82 (1999) 4114.
[91] Ch. Lienau, A. Richter, J.W. Tomm, Appl. Phys. A 64 (1997) 341.
[92] M.K. Herndon, A. Gupta, V. Kaydanov, R.T. Collins, Appl. Phys. Lett. 75 (1999) 3503.
[93] M.K. Herndon, W.C. Bradford, R.T. Collins, B.E. Hawkins, T.F. Kuech, D.J. Friedman, S.R. Kurtz, Appl. Phys. Lett. 77 (2000) 100.
[94] X.S. Xie, R.C. Dunn, Science 265 (1994) 361.
[95] S. Smith, B.G. Orr, R. Kopelman, T. Norris, Ultramicroscopy 57 (1995) 173.
[96] J. Levy, V. Nikitin, J.M. Kikkawa, D.D. Awschalom, N. Samarth, J. Appl. Phys. 79 (1996) 6095.
[97] A.H. LaRosa, C.L. Jahncke, H.D. Hallen, Ultramicroscopy 57 (1995) 303.
[98] A.H. La Rosa, B.I. Yakobson, H.H. Hallen, Appl. Phys. Lett. 70 (1997) 1656.
[99] A. Vertikov, M. Kuball, A.V. Nurmikko, H.J. Maris, Appl. Phys. Lett. 69 (1996) 2465.
[100] B.A. Nechay, U. Siegner, F. Morier-Genoud, A. Schertel, U. Keller, Appl. Phys. Lett. 74 (1999) 61.
[101] T. Guenther, V. Emiliani, F. Intonti, C. Lienau, T. Elsaesser, R. Notzel, K.H. Ploog, Appl. Phys. Lett. 75 (1999) 3500.
[102] C. Paulson, B. Hawkins, J. Sun, A.B. Ellis, L. McCaughan, T.F. Kuech, Appl. Phys. Lett. 77 (2000) 1943.
[103] C.L. Jahncke, M.A. Paesler, H.D. Hallen, Appl. Phys. Lett. 67 (1995) 2483.
[104] C.L. Jahncke, H.D. Hallen, Rev. Sci. Instrum. 68 (1997) 1759.
[105] E.J. Ayars, H.D. Hallen, Appl. Phys. Lett. 76 (2000) 3911.
[106] D. Zeisel, V. Deckert, R. Zenobi, T. Vo-Dinh, Chem. Phys. Lett. 283 (1998) 381.
[107] V. Deckert, D. Zeisel, R. Zenobi, T. Vo-Dinh, Anal. Chem. 70 (1998) 2646.
[108] M.S. Anderson, Appl. Phys. Lett. 76 (2000) 3130.
[109] B. Dragnea, J. Preusser, W. Schade, S. Leone, W.D. Hinsberg, J. Appl. Phys. 86 (1999) 2795.
[110] A. Cricenti, R. Generosi, P. Perfetti, G. Margaritondo, J. Almeida, J.M. Gilligan, N.H. Tolk, C. Coluzza, M. Spajer, D. Courjon, I.D. Aggarwal, Phys. Stat. Sol. (A) 175 (1999) 317.
[111] A. Lahrech, R. Bachelot, P. Gleyzes, A. Boccara, Appl. Phys. Lett. 71 (1997) 575.
[112] B. Knoll, F. Keilmann, Nature 399 (1999) 134.

[113] F. Keilmann, B. Knoll, A. Kramer, Phys. Stat. Sol. (B) 215 (1999) 849.
[114] E. Betzig, J.K. Trautman, J.S. Weiner, T.D. Harris, R. Wolfe, Appl. Opt. 31 (1992) 4563.
[115] E. Betzig, J.K. Trautman, Science 257 (1992) 189.
[116] E.B. McDaniel, J.W.P. Hsu, J. Appl. Phys. 80 (1996) 1085.
[117] G.A. Valaskovic, M. Holton, G.H. Morrison, J. Microsc. 179 (1995) 29.
[118] M. Vaez-Iravani, R. Toledo-Crow, Appl. Phys. Lett. 63 (1993) 138.
[119] K.W. Hipps, G.A. Crosby, J. Phys. Chem. 83 (1979) 555.
[120] S.N. Jasperson, S.E. Schnatterly, Rev. Sci. Instrum. 40 (1969) 761.
[121] D.A. Higgins, D.A. Vanden Bout, J. Kerimo, P.F. Barbara, J. Phys. Chem. 100 (1996) 13794.
[122] D.A. Vanden Bout, J. Kerimo, D.A. Higgins, P.F. Barbara, Acc. Chem. Res. 30 (1997) 204.
[123] Th. Lacoste, Th. Huser, R. Prioli, H. Heinzelmann, Ultramicroscopy 71 (1998) 333.
[124] V.K. Gupta, J.A. Kornfield, Rev. Sci. Instrum. 65 (1994) 2823.
[125] T.C. Oakberg, Linear Birefringence and Optical Rotation, Hinds Instruments Application Note, Hinds Instruments, Hillsboro, OR, 1993.
[126] G. Eggers, A. Rosenberger, N. Held, A. Munnemann, G. Guntherodt, P. Fumagalli, Ultramicroscopy 71 (1998) 249.
[127] C. Durkan, I.V. Shvets, J.C. Lodder, Appl. Phys. Lett. 70 (1997) 1323.
[128] P. Fumagalli, A. Rosenberger, G. Eggers, A. Munnemann, N. Held, G. Guntherodt, Appl. Phys. Lett. 72 (1998) 2803.
[129] B.L. Petersen, A. Bauer, G. Meyer, T. Crecelius, G. Kaindl, Appl. Phys. Lett. 73 (1998) 538.
[130] R.D. Grober, T.D. Harris, J.K. Trautman, E. Betzig, Rev. Sci. Instrum. 65 (1994) 626.
[131] H. Ghaemi, C. Gates, B. Goldberg, Ultramicroscopy 57 (1995) 165.
[132] W. Göhde, J. Tittel, Th. Basché, C. Bräuchle, U.C. Fischer, H. Fuchs, Rev. Sci. Instrum. 68 (1997) 2466.
[133] Y. Durand, J.C. Woehl, B. Viellerobe, W. Göhde, M. Orrit, Rev. Sci. Instrm. 70 (1999) 1318.
[134] H.F. Hess, E. Betzig, T.D. Harris, L.N. Pfeiffer, K.W. West, Science 264 (1994) 1740.
[135] V. Emiliani, C. Lienau, M. Hauert, G. Coli, M. DeGiorgi, R. Rinaldi, A. Passaseo, R. Cingolani, Phys. Rev. B 60 (1999) 13335.
[136] G. Nunes, D. Williams, J. Vac. Sci. Technol. B 13 (1995) 1063.
[137] G. Behme, A. Richter, M. Süptitz, Ch. Lienau, Rev. Sci. Instrum. 68 (1997) 3458.
[138] M.H. Gray, J.W.P. Hsu, Rev. Sci. Instrum. 70 (1999) 3355.
[139] J.W.P. Hsu, E.A. Fitzgerald, Y.H. Xie, P.J. Silverman, Appl. Phys. Lett. 65 (1994) 344.
[140] J.W.P. Hsu, E.A. Fitzgerald, Y.H. Xie, P.J. Silverman, J. Appl. Phys. 79 (1996) 7743.
[141] J.W.P. Hsu, M.H. Gray, Q. Xu, unpublished.
[142] Q. Xu, M.H. Gray, J.W.P. Hsu, J. Appl. Phys. 82 (1997) 748.
[143] M.H. Gray, J.W.P. Hsu, Appl. Phys. Lett. 76 (2000) 1294.
[144] Y.J. Mii, Y.H. Xie, E.A. Fitzgerald, D. Monroe, F.A. Thiel, B.E. Weir, L.C. Feldman, Appl. Phys. Lett. 59 (1991) 1611.
[145] Y.H. Xie, D. Monroe, E.A. Fitzgerald, P.J. Silverman, F.A. Thiel, G.P. Watson, Appl. Phys. Lett. 63 (1993) 2263.
[146] F. Schaffler, D. Tobben, H.J. Herzog, G. Albstreiter, B. Hollander, Semicond. Sci. Technol. 7 (1992) 260.
[147] E.A. Fitzgerald, Y.H. Xie, D. Monroe, P.J. Silverman, J.M. Kuo, A.R. Kortan, F.A. Thiel, B.E. Weir, J. Vac. Sci. Technol. B 10 (1992) 1807.
[148] E.A. Fitzgerald, Y.H. Xie, M.L. Green, D. Brasen, A.R. Kortan, J. Michel, Y.J. Mii, B.E. Weir, Appl. Phys. Lett. 59 (1991) 811.
[149] Y.H. Xie, E.A. Fitzgerald, P.J. Silverman, A.R. Kortan, B.E. Weir, J. Mater. Sci. Eng. B 14 (1992) 332.
[150] J.W.P. Hsu, E.A. Fitzgerald, Y.H. Xie, P.J. Silverman, M.J. Cardillo, Appl. Phys. Lett. 61 (1992) 1293.
[151] S.K. Buratto, J.W.P. Hsu, J.K. Trautman, E. Betzig, R.B. Bylsma, C.C. Bahr, M.J. Cardillo, Appl. Phys. Lett. 65 (1994) 2654.
[152] K. Karrai, G. Kolb, G. Abstreiter, A. Schmeller, Ultramicroscopy 61 (1995) 299.
[153] H. Fukuda, Y. Kadota, M. Ohtsu, Jpn. J. Appl. Phys. 38 (1999) L571.
[154] A.A. McDaniel, J.W.P. Hsu, A.M. Gabor, Appl. Phys. Lett. 70 (1997) 3555.
[155] C. Donolato, Appl. Phys. Lett. 34 (1979) 80.
[156] C. Donolato, Phys. Stat. Sol. (A) 66 (1981) 445.
[157] S.M. Sze, Physics of Semiconductor Devices, 2nd Edition, Wiley, New York, 1981 (Chapter 1).
[158] Z.J. Radzimski, T.Q. Zhou, A. Buczkowski, G.A. Rozgonyi, D. Finn, L.G. Hellwig, J.A. Ross, Appl. Phys. Lett. 60 (1992) 1096.
[159] W. Kittler, W. Seifert, Phys. Stat. Sol. (A) 138 (1993) 687.
[160] M. Kittler, C. Ulhaq-Bouillet, V. Higgs, J. Appl. Phys. 78 (1995) 4573.
[161] M.H. Gray, J.W.P. Hsu, unpublished.
[162] M.H. Gray, J.W.P. Hsu, L. Giovane, M.H. Bulsar, Phys. Rev. Lett. (in press).
[163] M.T. Bulsara, Ph.D. Thesis, Massachusetts Institute of Technology, 1998.
[164] B. Kabius, J.W. Seo, T. Amrein, U. Dahne, A. Scholen, M. Siegel, K. Urban, L. Schultz, Phys. C 231 (1994) 123.
[165] C. Traeholt, J.G. Wen, H.W. Zndbergen, Y. Shen, J.W.M. Hilgenkamp, Phys. C 230 (1994) 425.

[166] J.W. Seo, B. Kabius, U. Dahne, A. Scholen, K. Urban, Phys. C 245 (1995) 25.
[167] D.J. Miller, T.A. Roberts, J.H. Kang, J. Talvacchio, D.B. Buchholz, R.P.H. Chang, Appl. Phys. Lett. 66 (1995) 2561.
[168] D. Dimos, P. Chaudhari, J. Mannhart, F.K. LeGoues, Phys. Rev. Lett. 61 (1988) 219.
[169] D. Dimos, P. Chaudhari, J. Mannhart, Phys. Rev. B 41 (1990) 4038.
[170] E.B. McDaniel, S.C. Gausepohl, C.T. Li, M. Lee, J.W.P. Hsu, R.A. Rao, C.B. Eom, Appl. Phys. Lett. 70 (1997) 1882.
[171] J.W.P. Hsu, E.B. McDaniel, R.A. Rao, C.B. Eom, Mater. Res. Soc. Symp. Proc. 474 (1997) 91.
[172] E.B. McDaniel, J.W.P. Hsu, Mater. Res. Soc. Symp. Proc. 474 (1997) 131.
[173] E.B. McDaniel, J.W.P. Hsu, J. Appl. Phys. 84 (1998) 189.
[174] J.W.P. Hsu, E.B. McDaniel, A.L. Campillo, S.C. Gausepohl, M. Lee, R.A. Rao, C.B. Eom, IEEE Trans. Appl. Supercond. 9 (1999) 3413.
[175] E.B. McDaniel, J.W.P. Hsu, J. Appl. Phys. 81 (1997) 2488.
[176] E.B. McDaniel, Ph.D. Dissertation, University of Virginia, 1997.
[177] J.F. Nye, Physical Properties of Crystals, Clarendon Press, Oxford, 1985, Chapter XIII, p. 2.
[178] F. Gervais, in: E.D. Palik (Ed.), Handbook of Optical Constants of Solids II, Academic Press, Boston, 1991.
[179] J. Reintjes, M.B. Schulz, J. Appl. Phys. 39 (1968) 5254.
[180] S.Y. Shu, Z.Z. Kuo, D. Fong, J. Phys. (Paris) C 6 (1980) 186.
[181] K. Szot, W. Speier, J. Herion, Ch. Freiburg, Appl. Phys. A 64 (1997) 55.
[182] J. Weertman, J.R. Weertman, Elementary Dislocation Theory, Oxford University Press, Oxford, New York, 1992 (Chapter 2).
[183] C.B. Eom, J.Z. Sun, K. Yamamoto, A.F. Marshall, K.E. Luther, S.S. Laderman, T.H. Geballe, Appl. Phys. Lett. 55 (1989) 595.
[184] S. Nakamura, M. Senoh, S. Nagahama, N. Iwasa, T. Yamada, T. Matsushita, Y. Sugimoto, Appl. Phys. Lett. 69 (1996) 1568, and references therein
[185] S.J. Rosner, E.C. Carr, M.J. Ludowise, G. Girolami, H.I. Erikson, Appl. Phys. Lett. 70 (1997) 420.
[186] J. Neugebauer, C.G. Vande Walle, Appl. Phys. Lett. 69 (1996) 503.
[187] S. Chichibu, K. Wada, S. Nakamura, Appl. Phys. Lett. 71 (1997) 2346.
[188] J. Liu, N.R. Perkins, M.N. Horton, J.M. Redwing, M.A. Tischler, T.F. Kuech, Appl. Phys. Lett. 69 (1996) 3519.
[189] X. Li, P.W. Bohn, J.J. Coleman, Appl. Phys. Lett. 75 (1999) 4049.
[190] P.A. Crowell, D.K. Young, S. Keller, E.L. Hu, D.D. Awschalom, Appl. Phys. Lett. 72 (1998) 927.
[191] A. Vertikov, I. Ozedn, A.V. Nurmikko, Appl. Phys. Lett. 74 (1999) 850.
[192] A. Vertikov, I. Ozden, A.V. Nurmikko, J. Appl. Phys. 86 (1999) 4697.
[193] A. Vertikov, M. Kuball, A.V. Nurmikko, Y. Chen, S.Y. Wang, Appl. Phys. Lett. 72 (1998) 2645.
[194] A. Vertikov, A.V. Nurmikko, K. Doverspike, G. Bulman, J. Edmond, Appl. Phys. Lett. 73 (1998) 493.
[195] D. Gammon, E.S. Snow, B.V. Shanabrook, D.S. Katzer, D. Park, Phys. Rev. Lett. 76 (1996) 3005.
[196] J.K. Leong, C.C. Williams, J.M. Olson, Phys. Rev. B 56 (1997) 1472.
[197] B.M. Basol, V.K. Kapur, A. Halani, C.R. Leidholm, J. Sharp, J.R. Sites, A. Swartzlander, R. Matson, H. Ullal, J. Vac. Sci. Technol. A 14 (1996) 2251.
[198] Y. Toda, S. Shinomori, K. Suzuki, Y. Arakawa, Appl. Phys. Lett. 73 (1998) 517.
[199] Y. Toda, S. Shinomori, K. Suzuki, Y. Arakawa, Phys. Rev. B 58 (1998) R10147.
[200] C. Obermuller, A. Deisenrieder, G. Abstreiter, K. Karrai, S. Grosse, S. Manus, J. Feldmann, H. Lipsanen, M. Sopanen, J. Ahopelto, Appl. Phys. Lett. 74 (1999) 3200.
[201] C. Obermuller, A. Deisenrieder, G. Abstreiter, K. Karrai, S. Grosse, S. Manus, J. Feldmann, H. Lipsanen, M. Sopanen, J. Ahopelto, Appl. Phys. Lett. 75 (1999) 358.
[202] F. Flack, N. Samarth, V. Nikitin, P.A. Crowell, J. Shi, J. Levy, D.D. Awschalom, Phys. Rev. B 54 (1996) R17312.
[203] M. Issacson, J.A. Cline, H. Barshatzky, J. Vac. Sci. Technol. B 9 (1991) 3103.
[204] B.B. Goldberg, M.S. Unlu, W.D. Herzog, H.F. Ghaemi, E. Towe, IEEE J. Sel. Top. Quant. Electron. 1 (1995) 1073.
[205] Ch. Lienau, A. Richter, A. Klehr, T. Elsaesser, Appl. Phys. Lett. 69 (1996) 2471.
[206] D.K. Young, M.P. Mack, A.C. Abare, M. Hansen, L.A. Coldren, S.P. Denbaars, E.L. Hu, D.D. Awschalom, Appl. Phys. Lett. 74 (1999) 2349.
[207] I. Horsch, R. Kusche, O. Marti, B. Weigl, K.J. Ebeling, J. Appl. Phys. 79 (1996) 3831.
[208] J. Kim, D.E. Pride, J.T. Boyd, H.E. Jackson, Appl. Phys. Lett. 72 (1998) 3112.
[209] J. Kim, J.T. Boyd, H.E. Jackson, K.D. Choquette, Appl. Phys. Lett. 76 (2000) 526.
[210] W.D. Herzog, M.S. Unlu, B.B. Goldberg, G.H. Rhodes, C. Harder, Appl. Phys. Lett. 70 (1997) 688.
[211] G.H. Vander Rhodes, J.M. Pomeroy, M.S. Unlu, B.B. Goldberg, K.J. Knopp, D.H. Christensen, Appl. Phys. Lett. 72 (1998) 1811.
[212] J.A. DeAro, K.D. Weston, R.W. Herrick, P.M. Petroff, S.K. Buratto, Semicond. Sci. Technol. 13 (1998) 1364.
[213] A. Richter, J.W. Tomm, Ch. Lienau, J. Luft, Appl. Phys. Lett. 69 (1996) 3981.
[214] B. Hecht, A. Zajac, Optics, Addison-Wesley, Menlo Park, CA, 1974.
[215] D.J. Butler, K.A. Nugent, A. Roberts, J. Appl. Phys. 75 (1994) 2753.
[216] S.T. Huntington, K.A. Nugent, A. Roberts, P. Mulvaney, K.M. Lo, J. Appl. Phys. 82 (1997) 510.

[217] D.J. Butler, A. Horsfall, K.A. Nugent, A. Roberts, I.M. Bassett, K.M. Lo, J. Appl. Phys. 77 (1995) 5514.
[218] L. Dhar, H.J. Lee, E.J. Laskowski, S.K. Buratto, H.M. Presby, C. Narayanan, C.C. Bahr, P.J. Anthony, M.J. Cardillo, SPIE Proc. 2535 (1995) 120.
[219] A.G. Choo, H.E. Jackson, U. Thiel, G.N. De Brabander, J.T. Boyd, Appl. Phys. Lett. 65 (1994) 947.
[220] G.H. Vander Rhodes, B.B. Goldberg, M.S. Unlu, S.T. Chu, W. Pan, T. Paneko, Y. Kokobun, B.E. Little, Appl. Phys. Lett. 75 (1999) 2368.
[221] D.P. Tsai, C.W. Yang, S.Z. Lo, H.E. Jackson, Appl. Phys. Lett. 75 (1999) 1039.
[222] P.K. Tien, Rev. Mod. Phys. 49 (1977) 361.
[223] S. Bourzeix, J.M. Moison, F. Mignard, F. Barthe, A.C. Boccara, C. Licoppe, B. Mersali, M. Allovon, A. Bruno, Appl. Phys. Lett. 73 (1998) 1035.
[224] G.H. Vander Rhodes, B.B. Goldberg, M.S. Unlu, S.T. Chu, B. Little, unpublished.
[225] B.B. Goldberg, M.S. Unlu, G. Vander Rhodes, Mater. Res. Soc. Proc. 588 (2000) 3.
[226] M.L.M. Balistreri, D.J.W. Klunder, J.P. Korterik, F.C. Blom, A. Driessen, H.W.J.M. Hoekstra, L. Kuipers, N.F. van Hulst, Opt. Lett. 24 (1999) 1829.
[227] C. Peeters, E. Fluck, A.M. Otter, M.L.M. Balistreri, J.P. Korterik, L. Kuipers, N.F. van Hulst, Appl. Phys. Lett. 77 (2000) 142.
[228] S. Fan, I. Appelbaum, J.D. Joannopoulos, Appl. Phys. Lett. 75 (1999) 3461.
[229] P.L. Phillips, J.C. Knight, J.M. Pottage, G. Kakarantzas, P.St.J. Russell, Appl. Phys. Lett. 76 (2000) 541.
[230] M.L.M. Balistreri, J.P. Korterik, L. Kuipers, N.F. van Hulst, Phys. Rev. Lett. 85 (2000) 294.
[231] J.D. Joannopoulos, R.D. Meade, J.N. Winn, Photonic Crystals: Molding the Flow of Light, Princeton University Press, Princeton, NJ, 1995.
[232] A. Mekis, J.C. Chen, I. Kurland, S. Fan, P.R. Villeneuve, J.D. Joannopoulos, Phys. Rev. Lett. 77 (1996) 3787.
[233] J.S. Foresi, P.R. Villeneuve, J. Ferrera, E.R. Theon, G. Steinmeyer, S. Fan, J.D. Joannopoulos, L.C. Kimmerling, H.I. Smith, E.P. Ippen, Nature 390 (1997) 143.
[234] A. Scherer, O. Painter, B. D'Urso, R. Lee, A. Yariv, J. Vac. Sci. Technol. B 16 (1998) 3906.
[235] M. Meier, A. Mekis, A. Dodabalapur, A. Timko, R.E. Slusher, J.D. Joannopoulos, O Nalamasu, Appl. Phys. Lett. 74 (1999) 7.
[236] A. Mekis, S. Fan, J.D. Joannopoulos, Phys. Rev. B 58 (1998) 4809.
[237] E.B. McDaniel, J.W.P. Hsu, L.S. Goldner, R.J. Tonucci, E.L. Shirley, G.W. Bryant, Phys. Rev. B 55 (1997) 10878.
[238] G.H. Vander Rhodes, M.S. Unlu, B.B. Goldberg, J.M. Pomeroy, T.F. Krauss, IEE Proc. Optoelectron. 145 (1998) 379.
[239] P.L. Phillips, J.C. Knight, B.J. Mangan, P.St.J. Russell, M.D.B. Charlton, G.J. Parker, J. Appl. Phys. 85 (1999) 6337.
[240] A. Rosenberg, R.J. Tonucci, E.A. Bolden, Appl. Phys. Lett. 69 (1996) 2638.
[241] G.W. Bryant, E.L. Shirley, L.S. Goldner, E.B. McDaniel, J.W.P. Hsu, R.J. Tonucci, Phys. Rev. B 58 (1998) 2131.
[242] A.L. Campillo, C.A. White, J.W.P. Hsu, A. Rothenberg, J. Appl. Phys. (in press).
[243] P.R. Villeneuve, M. Piche, Phys. Rev. B 46 (1992) 4969.
[244] G.W. Bryant, private communications.
[245] A.L. Campillo, J.W.P. Hsu, unpublished.